Measurement of K0S and K∗0 in p + p, d + Au, and Cu + Cu collisions at √sNN = 200 GeV

(PHENIX Collaboration) Adare, A.; ...; Makek, Mihael; ...; Zolin, L.

Measurement of K^0_S and K^{*0} in $p + p$, $d +$ Au, and Cu + Cu collisions at $\sqrt{s_{NN}} = 200$ GeV

A. Adare,[13] S. Afanasiev,[32] C. Aidala,[14,45,46] N. N. Ajitanand,[64] Y. Akiba,[58,59] R. Akimoto,[12] H. Al-Bataineh,[52] J. Alexander,[64] M. Alfred,[25] A. Angerami,[14] K. Aoki,[37,58] N. Apadula,[30,65] L. Aphecetche,[66] Y. Aramaki,[12,58] R. Armendariz,[52] S. H. Aronson,[7] J. Asai,[59] H. Asano,[37,58] E. T. Atomssa,[38,65] R. Averbeck,[65] T. C. Awes,[54] B. Azmoun,[7] V. Babintsev,[26] M. Bai,[6] G. Baksay,[20] L. Baksay,[20] A. Baldisseri,[16] N. S. Bandara,[45] B. Bannier,[65] K. N. Barish,[8] P. D. Barnes,[41,*] B. Bassalleck,[51] A. T. Basye,[1] S. Bathe,[5,8,59] S. Batsouli,[54] V. Baublis,[57] C. Baumann,[47] A. Bazilevsky,[7] M. Beaumier,[8] S. Beckman,[13] S. Belikov,[7,*] R. Belmont,[46,70] R. Bennett,[65] A. Berdnikov,[61] Y. Berdnikov,[61] J. H. Bhom,[74] A. A. Bickley,[13] D. Black,[8] D. S. Blau,[36] J. G. Boissevain,[41] J. S. Bok,[52,74] H. Borel,[16] K. Boyle,[59,65] M. L. Brooks,[41] J. Bryslawskyj,[5] H. Buesching,[7] V. Bumazhnov,[26] G. Bunce,[7,59] S. Butsyk,[41,65] S. Campbell,[30,65] A. Caringi,[48] B. S. Chang,[74] J.-L. Charvet,[16] C.-H. Chen,[59,65] S. Chernichenko,[26] C. Y. Chi,[14] J. Chiba,[34] M. Chiu,[7,27] I. J. Choi,[27,74] J. B. Choi,[10] R. K. Choudhury,[4] P. Christiansen,[43] T. Chujo,[69,70] P. Chung,[64] A. Churyn,[26] O. Chvala,[8] V. Cianciolo,[54] Z. Citron,[65,72] C. R. Cleven,[22] B. A. Cole,[14] M. P. Comets,[55] Z. Conesa del Valle,[38] M. Connors,[65] P. Constantin,[41] M. Csanád,[18] T. Csörgő,[73] T. Dahms,[65] S. Dairaku,[37,58] I. Danchev,[70] K. Das,[21] A. Datta,[45,51] M. S. Daugherity,[1] G. David,[7] M. K. Dayananda,[22] M. B. Deaton,[1] K. DeBlasio,[51] K. Dehmelt,[20,65] H. Delagrange,[66] A. Denisov,[26] D. d'Enterria,[14] A. Deshpande,[59,65] E. J. Desmond,[7] K. V. Dharmawardane,[52] O. Dietzsch,[62] L. Ding,[30] A. Dion,[30,65] J. H. Do,[74] M. Donadelli,[62] O. Drapier,[38] A. Drees,[65] K. A. Drees,[6] A. K. Dubey,[72] J. M. Durham,[41,65] A. Durum,[26] D. Dutta,[4] V. Dzhordzhadze,[8] L. D'Orazio,[44] S. Edwards,[21] Y. V. Efremenko,[54] J. Egdemir,[65] F. Ellinghaus,[13] W. S. Emam,[8] T. Engelmore,[14] A. Enokizono,[40,54,58,60] H. En'yo,[58,59] S. Esumi,[69] K. O. Eyser,[8] B. Fadem,[48] N. Feege,[65] D. E. Fields,[51,59] M. Finger,[9,32] M. Finger, Jr.,[9,32] F. Fleuret,[38] S. L. Fokin,[36] Z. Fraenkel,[72,*] J. E. Frantz,[53,65] A. Franz,[7] A. D. Frawley,[21] K. Fujiwara,[58] Y. Fukao,[37,58] T. Fusayasu,[50] S. Gadrat,[42] C. Gal,[65] P. Gallus,[15] P. Garg,[3] I. Garishvili,[67] H. Ge,[65] F. Giordano,[27] A. Glenn,[13,40] H. Gong,[65] M. Gonin,[38] J. Gosset,[16] Y. Goto,[58,59] R. Granier de Cassagnac,[38] N. Grau,[2,14,30] S. V. Greene,[70] G. Grim,[41] M. Grosse Perdekamp,[27,59] Y. Gu,[64] T. Gunji,[12] H. Guragain,[22] H.-Å. Gustafsson,[43,*] T. Hachiya,[24,58] A. Hadj Henni,[66] C. Haegemann,[51] J. S. Haggerty,[7] K. I. Hahn,[19] H. Hamagaki,[12] J. Hamblen,[67] R. Han,[56] S. Y. Han,[19] J. Hanks,[14,65] H. Harada,[24] E. P. Hartouni,[40] K. Haruna,[24] S. Hasegawa,[31] E. Haslum,[43] R. Hayano,[12] X. He,[22] M. Heffner,[40] T. K. Hemmick,[65] T. Hester,[8] H. Hiejima,[27] J. C. Hill,[30] R. Hobbs,[51] M. Hohlmann,[20] R. S. Hollis,[8] W. Holzmann,[14,64] K. Homma,[24] B. Hong,[35] T. Horaguchi,[24,58,68] D. Hornback,[67] T. Hoshino,[24] S. Huang,[70] T. Ichihara,[58,59] R. Ichimiya,[58] H. Iinuma,[37,58] Y. Ikeda,[58,69] K. Imai,[31,37,58] Y. Imazu,[58] M. Inaba,[69] Y. Inoue,[58,60] A. Iordanova,[8] D. Isenhower,[1] L. Isenhower,[1] M. Ishihara,[58] T. Isobe,[12] M. Issah,[64,70] A. Isupov,[32] D. Ivanischev,[57] D. Ivanishchev,[57] Y. Iwanaga,[24] B. V. Jacak,[65] S. J. Jeon,[49] M. Jezghani,[22] J. Jia,[7,14,64] X. Jiang,[41] J. Jin,[14] O. Jinnouchi,[59] B. M. Johnson,[7] T. Jones,[1] E. Joo,[35] K. S. Joo,[49] D. Jouan,[55] D. S. Jumper,[1,27] F. Kajihara,[12] S. Kametani,[12,71] N. Kamihara,[58] J. Kamin,[65] M. Kaneta,[59] J. H. Kang,[74] J. S. Kang,[23] H. Kanou,[58,68] J. Kapustinsky,[41] K. Karatsu,[37,58] M. Kasai,[58,60] D. Kawall,[45,59] M. Kawashima,[58,60] A. V. Kazantsev,[36] T. Kempel,[30] J. A. Key,[51] V. Khachatryan,[65] A. Khanzadeev,[57] K. Kihara,[69] K. M. Kijima,[24] J. Kikuchi,[71] A. Kim,[19] B. I. Kim,[35] C. Kim,[35] D. H. Kim,[19,49] D. J. Kim,[33,74] E. Kim,[63] E.-J. Kim,[10] H.-J. Kim,[74] M. Kim,[63] Y.-J. Kim,[27] Y. K. Kim,[23] E. Kinney,[13] Á. Kiss,[18] E. Kistenev,[7] A. Kiyomichi,[58] J. Klatsky,[21] J. Klay,[40] C. Klein-Boesing,[47] D. Kleinjan,[8] P. Kline,[65] T. Koblesky,[13] L. Kochenda,[57] V. Kochetkov,[26] M. Kofarago,[18] B. Komkov,[57] M. Konno,[69] J. Koster,[27,59] D. Kotchetkov,[8] D. Kotov,[57,61] A. Kozlov,[72] A. Král,[15] A. Kravitz,[14] J. Kubart,[9,29] G. J. Kunde,[41] N. Kurihara,[12] K. Kurita,[58,60] M. Kurosawa,[58,59] M. J. Kweon,[35] Y. Kwon,[67,74] G. S. Kyle,[52] R. Lacey,[64] Y. S. Lai,[14] J. G. Lajoie,[30] A. Lebedev,[30] D. M. Lee,[41] J. Lee,[19] K. B. Lee,[35,41] K. S. Lee,[35] M. K. Lee,[74] S. H. Lee,[65] T. Lee,[63] M. J. Leitch,[41] M. A. L. Leite,[62] M. Leitgab,[27] B. Lenzi,[62] X. Li,[11] P. Lichtenwalner,[48] P. Liebing,[59] S. H. Lim,[74] L. A. Linden Levy,[13] T. Liška,[15] A. Litvinenko,[32] H. Liu,[41] M. X. Liu,[41] B. Love,[70] D. Lynch,[7] C. F. Maguire,[70] Y. I. Makdisi,[6] M. Makek,[72,75] A. Malakhov,[32] M. D. Malik,[51] A. Manion,[65] V. I. Manko,[36] E. Mannel,[7,14] Y. Mao,[56,58] L. Mašek,[9,29] H. Masui,[69] F. Matathias,[14] M. McCumber,[41,65] P. L. McGaughey,[41] D. McGlinchey,[13,21] C. McKinney,[27] N. Means,[65] A. Meles,[52] M. Mendoza,[8] B. Meredith,[14,27] Y. Miake,[69] T. Mibe,[34] A. C. Mignerey,[44] P. Mikeš,[9,29] K. Miki,[58,69] A. J. Miller,[1] T. E. Miller,[70] A. Milov,[7,65,72] S. Mioduszewski,[7] D. K. Mishra,[4] M. Mishra,[3] J. T. Mitchell,[7] M. Mitrovski,[64] S. Miyasaka,[58,68] S. Mizuno,[58,69] A. K. Mohanty,[4] P. Montuenga,[27] H. J. Moon,[49] T. Moon,[74] Y. Morino,[12] A. Morreale,[8] D. P. Morrison,[7,†] T. V. Moukhanova,[36] D. Mukhopadhyay,[70] T. Murakami,[37,58] J. Murata,[58,60] A. Mwai,[64] S. Nagamiya,[34,58] Y. Nagata,[69] J. L. Nagle,[13,‡] M. Naglis,[72] M. I. Nagy,[18,73] I. Nakagawa,[58,59] H. Nakagomi,[58,69] Y. Nakamiya,[24] K. R. Nakamura,[37,58] T. Nakamura,[24,58] K. Nakano,[58,68] S. Nam,[19] C. Nattrass,[67] P. K. Netrakanti,[4] J. Newby,[40] M. Nguyen,[65] M. Nihashi,[24,58] T. Niida,[69] B. E. Norman,[41] R. Nouicer,[7,59] N. Novitzky,[33] A. S. Nyanin,[36] C. Oakley,[22] E. O'Brien,[7] S. X. Oda,[12] C. A. Ogilvie,[30] H. Ohnishi,[58] M. Oka,[69] K. Okada,[59] O. O. Omiwade,[1] Y. Onuki,[58] J. D. Orjuela Koop,[13] A. Oskarsson,[43] M. Ouchida,[24,58] H. Ozaki,[69] K. Ozawa,[12,34] R. Pak,[7] D. Pal,[70] A. P. T. Palounek,[41] V. Pantuev,[28,65] V. Papavassiliou,[52] I. H. Park,[19] J. Park,[63] S. Park,[63] S. K. Park,[35] W. J. Park,[35] S. F. Pate,[52] L. Patel,[22] M. Patel,[30] H. Pei,[30] J.-C. Peng,[27] H. Pereira,[16] D. V. Perepelitsa,[7,14] G. D. N. Perera,[52] V. Peresedov,[32] D.Yu. Peressounko,[36] J. Perry,[30] R. Petti,[65] C. Pinkenburg,[7] R. Pinson,[1] R. P. Pisani,[7] M. Proissl,[65] M. L. Purschke,[7] A. K. Purwar,[41] H. Qu,[22] J. Rak,[33,51] A. Rakotozafindrabe,[38] I. Ravinovich,[72] K. F. Read,[54,67] S. Rembeczki,[20] M. Reuter,[65] K. Reygers,[47] D. Reynolds,[64] V. Riabov,[57] Y. Riabov,[57,61] E. Richardson,[44] N. Riveli,[53] D. Roach,[70] G. Roche,[42] S. D. Rolnick,[8] A. Romana,[38,*] M. Rosati,[30] C. A. Rosen,[13] S. S. E. Rosendahl,[43] P. Rosnet,[42] Z. Rowan,[5] J. G. Rubin,[46] P. Rukoyatkin,[32] P. Ružička,[29] V. L. Rykov,[58] B. Sahlmueller,[47,65] N. Saito,[34,37,58,59] T. Sakaguchi,[7] S. Sakai,[69] K. Sakashita,[58,68] H. Sakata,[24] H. Sako,[31] V. Samsonov,[57]

S. Sano,[12,71] M. Sarsour,[22] S. Sato,[31,34] T. Sato,[69] S. Sawada,[34] B. Schaefer,[70] B. K. Schmoll,[67] K. Sedgwick,[8] J. Seele,[13,59] R. Seidl,[27,58,59] V. Semenov,[26] A. Sen,[67] R. Seto,[8] P. Sett,[4] A. Sexton,[44] D. Sharma,[65,72] I. Shein,[26] A. Shevel,[57,64] T.-A. Shibata,[58,68] K. Shigaki,[24] M. Shimomura,[30,69] K. Shoji,[37,58] P. Shukla,[4] A. Sickles,[7,65] C. L. Silva,[30,41,62] D. Silvermyr,[54] C. Silvestre,[16] K. S. Sim,[35] B. K. Singh,[3] C. P. Singh,[3] V. Singh,[3] S. Skutnik,[30] M. Slunečka,[9,32] A. Soldatov,[26] R. A. Soltz,[40] W. E. Sondheim,[41] S. P. Sorensen,[67] I. V. Sourikova,[7] F. Staley,[16] P. W. Stankus,[54] E. Stenlund,[43] M. Stepanov,[45,52] A. Ster,[73] S. P. Stoll,[7] T. Sugitate,[24] C. Suire,[55] A. Sukhanov,[7] T. Sumita,[58] J. Sun,[65] J. Sziklai,[73] T. Tabaru,[59] S. Takagi,[69] E. M. Takagui,[62] A. Takahara,[12] A. Taketani,[58,59] R. Tanabe,[69] Y. Tanaka,[50] S. Taneja,[65] K. Tanida,[37,58,59,63] M. J. Tannenbaum,[7] S. Tarafdar,[3,72] A. Taranenko,[64] P. Tarján,[17] H. Themann,[65] D. Thomas,[1] T. L. Thomas,[51] A. Timilsina,[30] T. Todoroki,[58,69] M. Togawa,[37,58,59] A. Toia,[65] J. Tojo,[58] L. Tomášek,[29] M. Tomášek,[15] H. Torii,[24,58] M. Towell,[1] R. Towell,[1] R. S. Towell,[1] V-N. Tram,[38] I. Tserruya,[72] Y. Tsuchimoto,[24] C. Vale,[7,30] H. Valle,[70] H. W. van Hecke,[41] M. Vargyas,[73] E. Vazquez-Zambrano,[14] A. Veicht,[27] J. Velkovska,[70] R. Vértesi,[17,73] A. A. Vinogradov,[36] M. Virius,[15] V. Vrba,[15,29] E. Vznuzdaev,[57] M. Wagner,[37,58] D. Walker,[65] X. R. Wang,[52] D. Watanabe,[24] K. Watanabe,[69] Y. Watanabe,[58,59] Y. S. Watanabe,[34] F. Wei,[30,52] R. Wei,[64] J. Wessels,[47] S. Whitaker,[30] S. N. White,[7] D. Winter,[14] S. Wolin,[27] C. L. Woody,[7] R. M. Wright,[1] M. Wysocki,[13,54] B. Xia,[53] W. Xie,[59] L. Xue,[22] S. Yalcin,[65] Y. L. Yamaguchi,[12,58,71] K. Yamaura,[24] R. Yang,[27] A. Yanovich,[26] Z. Yasin,[8] J. Ying,[22] S. Yokkaichi,[58,59] I. Yoon,[63] Z. You,[56] G. R. Young,[54] I. Younus,[39,51] I. E. Yushmanov,[36] W. A. Zajc,[14] O. Zaudtke,[47] A. Zelenski,[6] C. Zhang,[54] S. Zhou,[11] J. Zimányi,[73,*] and L. Zolin[32]

(PHENIX Collaboration)

[1]*Abilene Christian University, Abilene, Texas 79699, USA*

[2]*Department of Physics, Augustana College, Sioux Falls, South Dakota 57197, USA*

[3]*Department of Physics, Banaras Hindu University, Varanasi 221005, India*

[4]*Bhabha Atomic Research Centre, Bombay 400 085, India*

[5]*Baruch College, City University of New York, New York, New York, 10010, USA*

[6]*Collider-Accelerator Department, Brookhaven National Laboratory, Upton, New York 11973-5000, USA*

[7]*Physics Department, Brookhaven National Laboratory, Upton, New York 11973-5000, USA*

[8]*University of California-Riverside, Riverside, California 92521, USA*

[9]*Charles University, Ovocný trh 5, Praha 1, 116 36, Prague, Czech Republic*

[10]*Chonbuk National University, Jeonju, 561-756, Korea*

[11]*Science and Technology on Nuclear Data Laboratory, China Institute of Atomic Energy, Beijing 102413, People's Republic of China*

[12]*Center for Nuclear Study, Graduate School of Science, University of Tokyo, 7-3-1 Hongo, Bunkyo, Tokyo 113-0033, Japan*

[13]*University of Colorado, Boulder, Colorado 80309, USA*

[14]*Columbia University, New York, New York 10027 and Nevis Laboratories, Irvington, New York 10533, USA*

[15]*Czech Technical University, Zikova 4, 166 36 Prague 6, Czech Republic*

[16]*Dapnia, CEA Saclay, F-91191, Gif-sur-Yvette, France*

[17]*Debrecen University, H-4010 Debrecen, Egyetem tér 1, Hungary*

[18]*ELTE, Eötvös Loránd University, H-1117 Budapest, Pázmány P. s. 1/A, Hungary*

[19]*Ewha Womans University, Seoul 120-750, Korea*

[20]*Florida Institute of Technology, Melbourne, Florida 32901, USA*

[21]*Florida State University, Tallahassee, Florida 32306, USA*

[22]*Georgia State University, Atlanta, Georgia 30303, USA*

[23]*Hanyang University, Seoul 133-792, Korea*

[24]*Hiroshima University, Kagamiyama, Higashi-Hiroshima 739-8526, Japan*

[25]*Department of Physics and Astronomy, Howard University, Washington, DC 20059, USA*

[26]*IHEP Protvino, State Research Center of Russian Federation, Institute for High Energy Physics, Protvino, 142281, Russia*

[27]*University of Illinois at Urbana-Champaign, Urbana, Illinois 61801, USA*

[28]*Institute for Nuclear Research of the Russian Academy of Sciences, prospekt 60-letiya Oktyabrya 7a, Moscow 117312, Russia*

[29]*Institute of Physics, Academy of Sciences of the Czech Republic, Na Slovance 2, 182 21 Prague 8, Czech Republic*

[30]*Iowa State University, Ames, Iowa 50011, USA*

[31]*Advanced Science Research Center, Japan Atomic Energy Agency, 2-4 Shirakata Shirane, Tokai-mura, Naka-gun, Ibaraki-ken 319-1195, Japan*

[32]*Joint Institute for Nuclear Research, 141980 Dubna, Moscow Region, Russia*

[33]*Helsinki Institute of Physics and University of Jyväskylä, P.O. Box 35, FI-40014 Jyväskylä, Finland*

[34]*KEK, High Energy Accelerator Research Organization, Tsukuba, Ibaraki 305-0801, Japan*

[35]*Korea University, Seoul, 136-701, Korea*

[36]*Russian Research Center "Kurchatov Institute," Moscow, 123098 Russia*

[37]*Kyoto University, Kyoto 606-8502, Japan*

[38]*Laboratoire Leprince-Ringuet, Ecole Polytechnique, CNRS-IN2P3, Route de Saclay, F-91128 Palaiseau, France*

[39]*Physics Department, Lahore University of Management Sciences, Lahore 54792, Pakistan*

[40]*Lawrence Livermore National Laboratory, Livermore, California 94550, USA*

[41]*Los Alamos National Laboratory, Los Alamos, New Mexico 87545, USA*
[42]*LPC, Université Blaise Pascal, CNRS-IN2P3, Clermont-Fd, 63177 Aubiere Cedex, France*
[43]*Department of Physics, Lund University, Box 118, SE-221 00 Lund, Sweden*
[44]*University of Maryland, College Park, Maryland 20742, USA*
[45]*Department of Physics, University of Massachusetts, Amherst, Massachusetts 01003-9337, USA*
[46]*Department of Physics, University of Michigan, Ann Arbor, Michigan 48109-1040, USA*
[47]*Institut fur Kernphysik, University of Muenster, D-48149 Muenster, Germany*
[48]*Muhlenberg College, Allentown, Pennsylvania 18104-5586, USA*
[49]*Myongji University, Yongin, Kyonggido 449-728, Korea*
[50]*Nagasaki Institute of Applied Science, Nagasaki-shi, Nagasaki 851-0193, Japan*
[51]*University of New Mexico, Albuquerque, New Mexico 87131, USA*
[52]*New Mexico State University, Las Cruces, New Mexico 88003, USA*
[53]*Department of Physics and Astronomy, Ohio University, Athens, Ohio 45701, USA*
[54]*Oak Ridge National Laboratory, Oak Ridge, Tennessee 37831, USA*
[55]*IPN-Orsay, Universite Paris Sud, CNRS-IN2P3, BP1, F-91406 Orsay, France*
[56]*Peking University, Beijing 100871, People's Republic of China*
[57]*PNPI, Petersburg Nuclear Physics Institute, Gatchina, Leningrad region 188300, Russia*
[58]*RIKEN Nishina Center for Accelerator-Based Science, Wako, Saitama 351-0198, Japan*
[59]*RIKEN BNL Research Center, Brookhaven National Laboratory, Upton, New York 11973-5000, USA*
[60]*Physics Department, Rikkyo University, 3-34-1 Nishi-Ikebukuro, Toshima, Tokyo 171-8501, Japan*
[61]*Saint Petersburg State Polytechnic University, St. Petersburg, 195251 Russia*
[62]*Universidade de São Paulo, Instituto de Física, Caixa Postal 66318, São Paulo CEP05315-970, Brazil*
[63]*Department of Physics and Astronomy, Seoul National University, Seoul 151-742, Korea*
[64]*Chemistry Department, Stony Brook University, SUNY, Stony Brook, New York 11794-3400, USA*
[65]*Department of Physics and Astronomy, Stony Brook University, SUNY, Stony Brook, New York 11794-3800, USA*
[66]*SUBATECH (Ecole des Mines de Nantes, CNRS-IN2P3, Université de Nantes) BP 20722-44307, Nantes, France*
[67]*University of Tennessee, Knoxville, Tennessee 37996, USA*
[68]*Department of Physics, Tokyo Institute of Technology, Oh-okayama, Meguro, Tokyo 152-8551, Japan*
[69]*Institute of Physics, University of Tsukuba, Tsukuba, Ibaraki 305, Japan*
[70]*Vanderbilt University, Nashville, Tennessee 37235, USA*
[71]*Waseda University, Advanced Research Institute for Science and Engineering, 17 Kikui-cho, Shinjuku-ku, Tokyo 162-0044, Japan*
[72]*Weizmann Institute, Rehovot 76100, Israel*
[73]*Institute for Particle and Nuclear Physics, Wigner Research Centre for Physics, Hungarian Academy of Sciences (Wigner RCP, RMKI) H-1525 Budapest 114, PO Box 49, Budapest, Hungary*
[74]*Yonsei University, IPAP, Seoul 120-749, Korea*
[75]*University of Zagreb, Faculty of Science, Department of Physics, Bijenička 32, HR-10002 Zagreb, Croatia*
(Received 23 May 2014; published 7 November 2014)

The PHENIX experiment at the Relativistic Heavy Ion Collider has performed a systematic study of K^0_S and K^{*0} meson production at midrapidity in $p + p$, $d +$ Au, and Cu + Cu collisions at $\sqrt{s_{NN}} = 200$ GeV. The K^0_S and K^{*0} mesons are reconstructed via their $K^0_S \to \pi^0(\to \gamma\gamma)\pi^0(\to \gamma\gamma)$ and $K^{*0} \to K^{\pm}\pi^{\mp}$ decay modes, respectively. The measured transverse-momentum spectra are used to determine the nuclear modification factor of K^0_S and K^{*0} mesons in $d +$ Au and Cu + Cu collisions at different centralities. In the $d +$ Au collisions, the nuclear modification factor of K^0_S and K^{*0} mesons is almost constant as a function of transverse momentum and is consistent with unity, showing that cold-nuclear-matter effects do not play a significant role in the measured kinematic range. In Cu + Cu collisions, within the uncertainties no nuclear modification is registered in peripheral collisions. In central collisions, both mesons show suppression relative to the expectations from the $p + p$ yield scaled by the number of binary nucleon-nucleon collisions in the Cu + Cu system. In the p_T range 2–5 GeV/c, the strange mesons (K^0_S, K^{*0}) similarly to the ϕ meson with hidden strangeness, show an intermediate suppression between the more suppressed light quark mesons (π^0) and the nonsuppressed baryons (p, $\bar{p}$). At higher transverse momentum, $p_T > 5$ GeV/c, production of all particles is similarly suppressed by a factor of $\approx$2.

DOI: 10.1103/PhysRevC.90.054905 PACS number(s): 25.75.Dw

I. INTRODUCTION

At very high energy densities, exceeding approximately 1 GeV/fm^3, quantum chromodynamics predicts a phase transition from ordinary hadronic nuclear matter to a new

*Deceased
†PHENIX Cospokesperson: morrison@bnl.gov
‡PHENIX Cospokesperson: jamie.nagle@colorado.edu

state of matter where the degrees of freedom are quarks and gluons [1]. This state of matter exhibits very strong coupling between its constituents and is thus called the strongly coupled quark-gluon plasma (sQGP) [2]. Matter at such high energy density can be produced in laboratory conditions by colliding heavy nuclei at relativistic energies. Many measurements are available from experiments at the Relativistic Heavy Ion Collider (RHIC) and the Large Hadron Collider (LHC) [3].

High-momentum penetrating probes are among the observables attracting primary attention. Highly energetic partons traversing the sQGP medium suffer significant energy loss [4,5], leading to modification of the fragmentation functions [6] and softening of the measured transverse momentum (p_T) distribution. The softening of the spectrum is quantified by the "nuclear modification factor" (R_{AB}) defined as

$$R_{AB} = \frac{d^2N_{AB}/dydp_T}{N_{\rm coll} \times d^2N_{pp}/dydp_T}, \quad (1)$$

where the numerator is the per-event yield of particle production in $A + B$ (heavy-ion) collisions, measured as a function of p_T, $d^2N_{pp}/dydp_T$ is the per-event yield of the same process in $p + p$ collisions, and $N_{\rm coll}$ is the number of nucleon-nucleon collisions in the $A + B$ system [7,8]. R_{AB} different from unity is a manifestation of medium effects. However, to untangle final-state effects, such as energy loss, from possible contributions of cold nuclear matter and initial-state effects (e.g., shadowing [9] and the Cronin effect [10]), the nuclear modification factor must also be measured in systems like $p + A$ or $d + A$.

A significant suppression of hadrons produced in heavy-ion collisions was first measured at RHIC [7,11–19] and recently at the LHC [20,21] also with fully reconstructed jets [22–24]. In central Au + Au collisions at RHIC, R_{AB} of hadrons reaches a maximum suppression of a factor of ∼5 at $p_T \sim 5$ GeV/c [12,14,15,25]. At higher p_T, the suppression is found to be independent of the particle type, mesons or baryons, and their quark flavor content [26–28]. In central Pb + Pb collisions at the LHC, the suppression reaches a factor of ∼7 at $p_T \sim$ 6–7 GeV/c [20,21]. At higher p_T, the R_{AB} starts to increase reaching a value of 0.5 at $p_T > 40$ GeV/c.

In the intermediate p_T range ($2 < p_T < 5$ GeV/c), mesons containing light quarks (π, η) exhibit suppression [14,29], whereas protons show very little or no suppression [29–31]. Other processes, such as the Cronin effect [10], strong radial flow [32], and recombination effects [33] have been invoked to explain the differences between mesons and baryons in this momentum range. Recent results obtained at the LHC in p + Pb collisions [34–36] and at RHIC in d + Au collisions [29,37] suggest that collective effects might be present even in small systems and can significantly modify the particle properties in the intermediate transverse momentum range.

Measurements of particles with different quark content provide additional constraints on the models of collective behavior, parton energy loss, and parton recombination. Experimental measurements of particles containing strange quarks are important to find out whether flow or recombination mechanisms boost strange hadron production at intermediate p_T and to understand their suppression at high p_T. In heavy-ion collisions, the ϕ meson [15] shows at high p_T the same suppression as particles containing only u and d quarks; however, at intermediate p_T it is less suppressed than the π meson. However, the η meson, which has a significant strange quark content, is suppressed at the same level as π meson in the p_T range from 2 to 10 GeV/c [14]. Open questions concern which physics mechanism prevails in the intermediate p_T region and which processes are responsible for the suppression of particles with strange quark content.

TABLE I. Summary of centrality bins and measured p_T ranges for the K^0_S and K^{*0} studies.

	Collision system	Centrality bins (%)	Measured p_T range (GeV/c)
K^0_S	d + Au	0–20, 20–40, 40–60, 60–88	2.0–13.0
	Cu + Cu	0–20, 20–60, 60–94	3.0–12.0
K^{*0}	$p + p$	–	1.1–8.0
	d + Au	0–20, 20–40, 40–60, 60–88	1.1–8.5
	Cu + Cu	0–20, 20–40, 40–60, 60–94	1.4–8.0

This article presents results of the K^0_S and K^{*0} meson production as a function of p_T at midrapidity in $p + p$, d + Au, and Cu + Cu collisions at $\sqrt{s_{NN}} = 200$ GeV. The present measurements significantly extend the p_T reach of the previous PHENIX results on the measurement of K^0_S meson in $p + p$ collisions [38]. The K^0_S meson is reconstructed via the $K^0_S \to \pi^0(\to \gamma\gamma)\pi^0(\to \gamma\gamma)$ decay mode. The K^{*0} and $\overline{K^{*0}}$ mesons are reconstructed via the $K^{*0} \to K^+\pi^-$ and $\overline{K^{*0}} \to K^-\pi^+$ decay modes, respectively. The yields measured for the K^{*0} and $\overline{K^{*0}}$ mesons are averaged together and denoted as K^{*0}. The invariant transverse momentum spectra for K^0_S mesons are measured over the p_T range of 2–13 (3–12) GeV/c in the d + Au (Cu + Cu) collision systems. The K^{*0} meson spectra are measured in the p_T range from 1.1 up to 8–8.5 GeV/c, depending on the collision system. The measurements extend the momentum coverage of the previously published results by the STAR Collaboration [39–41]. The nuclear modification factors are obtained for both particles in d + Au and Cu + Cu collisions at different centralities and are compared with those of the ϕ and π^0 mesons. The measured p_T ranges and the centrality bins used in the different systems are listed in Table I.

The paper is organized as follows. The next section gives a brief description of the PHENIX detector. The analysis procedures used to measure K^0_S and K^{*0} mesons are described in Sec. III. The results, including the invariant p_T distributions and R_{AB}, are given in Sec. IV. A summary is given in Sec. V.

II. PHENIX DETECTOR

A detailed description of the PHENIX detector can be found in Ref. [42]. The analysis reported here is performed using the two central-arm spectrometers, each covering an azimuthal angle $\phi = \pi/2$ and pseudorapidity $|\eta| < 0.35$ [43] at midrapidity. Each arm comprises a drift chamber (DC), two or three layers of pad chambers (PCs), a ring-imaging Čerenkov (RICH) detector, an electromagnetic calorimeter

(EMCal), and a time-of-flight (TOF) detector. This analysis uses the east arm of the TOF detector that covers $\pi/4$ in ϕ.

The global event information is provided by the beam-beam counters (BBCs) [44], which are used for event triggering, collision time determination, measurement of the vertex position along the beam axis, and the centrality determination [8,45]. The typical vertex position resolution of the BBC depends on the track multiplicity and varies from ∼1.1 cm in $p+p$ collisions to ∼3 mm in central Au + Au collisions.

Track reconstruction in PHENIX is provided by two detectors: DC and PC [43]. The DC and the first layer of the PC (PC1) form the inner tracking system, whereas PC2 and PC3 form the outer tracker. The DC is a multiwire gaseous detector located outside the magnetic field between the radii of 2.02 and 2.48 m in each PHENIX arm. The DC measures the track position with an angular resolution of ∼0.8 mrad in the bending plane perpendicular to the beam axis. A combinatorial Hough transform technique [46] is used to determine the track direction in azimuth and its bending angle in the axial magnetic field of the central magnet [47]. The track-reconstruction algorithm approximates all tracks in the volume of the DC with straight lines and assumes their origin at the collision vertex. This information is then combined with the hit information in PC1, which immediately follows the DC along the particle tracks. PC1 provides the z-coordinate information with a spatial resolution of $\sigma_z \sim 1.7$ mm. The resulting momentum resolution for charged particles with $p_T > 0.2$ GeV/c is $\delta p/p = 0.7 \oplus 1.1\% p$ (GeV/c), where the first term represents multiple scattering and the second term is attributable to the intrinsic angular resolution of the DC. Matching the tracks to hits in PC2 and PC3 located at radii of 4.2 and 5.0 m, respectively, helps to reject secondary tracks that originate either from decays of long-lived hadrons or from interactions with the detector material. Detailed information on the PHENIX tracking can be found in Refs. [43,48].

The TOF detector [49] identifies charged hadrons: pions, kaons, and protons. It is located at a radial distance of 5.06 m from the interaction point in the east central arm. The total timing resolution of TOF east is 130 ps, which includes the start time determination from the BBC. This allows for a 2.6σ π/K separation up to $p_T \simeq 2.5$ GeV/c and K/p separation up to $p_T = 4.5$ GeV/c using an asymmetric particle-identification (PID) cut, as described in Ref. [50].

The EMCal [51] uses lead-scintillator (PbSc) and lead-glass (PbGl) technologies and measures the position and energy of electrons and photons. It also provides a trigger on rare events with high momentum photons. The EMCal covers the full acceptance of the central spectrometers and is divided into eight sectors in azimuth. Six PbSc sectors are located at a radial distance of 5.1 m from the beamline and comprise 15 552 PbSc sandwich towers with cross section of 5.5×5.5 cm^2 and depth of 18 radiation lengths (X_0). Two PbGl sectors are located at a distance of 5 m and comprise 9216 towers of 4×4 cm^2 and a depth of $14.3X_0$. Most electromagnetic showers extend over several towers. Groups of adjacent towers with signals above a threshold that are associated with the same shower form an EMCal cluster. The energy resolution of the PbSc (PbGl) calorimeter is $\delta E/E = 2.1(0.8)\% \oplus 8.1(5.9)/\sqrt{E[\mathrm{GeV}]}\%$. The spatial resolution of the PbSc (PbGl) calorimeter reaches $\sigma(E) = 1.55(0.2) \oplus 5.74(8.4)/\sqrt{E[\mathrm{GeV}]}$ mm for particles at normal incidence.

Analyses presented in this paper use both the minimum bias (MB) and the rare-event, EMCal-RICH trigger (ERT). For $p+p$, $d+$Au, and Cu + Cu collisions, the MB trigger requires a coincidence of at least one channel firing on each side of the BBC. It further requires the vertex position along the beam axis z, as determined from the BBC timing information, to be within 38 cm of the nominal center of the interaction region. Photon ERT utilizes the EMCal to select events with at least one registered high-p_T photon or electron. For every EMCal supermodule [51], the ERT sums the registered energy in adjacent 4×4 EMCal towers. This trigger is used to collect samples for the K^0_S meson analysis. The trigger fires if the summed energy exceeds the 1.4- and 2.8-GeV thresholds in $d+$Au and Cu + Cu collisions, respectively. The calculation of the ERT efficiency for photons and K^0_S mesons is described in Sec. III C.

III. ANALYSIS PROCEDURE

This section describes the analysis procedure for the measurement of the K^0_S meson and K^{*0} meson transverse momentum spectra. The measurements are done using the data sets collected by the PHENIX experiment in the 2005 ($p+p$ and Cu + Cu) and in the 2008 ($d+$Au) physics runs. The data samples used in the analysis correspond to integrated luminosities of 3.78 pb^{-1} in $p+p$, 81 nb^{-1} in $d+$Au, and 3.06 nb^{-1} in Cu + Cu collision systems. The mesons are reconstructed via the decay modes $K^0_S \to \pi^0(\to \gamma\gamma)\pi^0(\to \gamma\gamma)$ and $K^{*0} \to K^{\pm}\pi^{\mp}$. The MB-triggered data samples are used for the K^{*0} meson study in $p+p$, $d+$Au, and Cu + Cu systems. The K^0_S meson measurements are done using both the MB and ERT-triggered data samples in $d+$Au and Cu + Cu collisions. The MB samples provide the measurements at low and intermediate p_T. The low p_T reach of these measurements is limited by the rapidly decreasing signal-to-background ratio and subsequent difficulties in the extraction of the K^0_S meson raw yield. The ERT-triggered data give access to intermediate- and high-p_T production of K^0_S mesons owing to larger sampled luminosities. In the overlap region, results obtained with the MB and ERT data samples are found to be in very good agreement. For the final K^0_S meson production spectrum in $d+$Au (Cu + Cu) collisions, the MB results are used up to 4 (5) GeV/c and the ERT results are used at higher transverse momenta. Details about the K^0_S meson measurement in $p+p$ collisions can be found in Ref. [38].

A. Reconstruction of K^0_S meson invariant mass

The K^0_S meson with a lifetime of $c\tau \sim 2.7$-cm decays to two π^0 mesons with a branching ratio BR = 30.69 ± 0.05% [52]. The neutral pions further decay into two photons with BR = 98.823 ± 0.034% [52]. The π^0 mesons are measured by combining the pair of photon clusters reconstructed in the EMCal. The energy of the clusters is measured in the EMCal and momentum components are calculated assuming that the particle originates at the event vertex. Besides electromagnetic showers created by photons and electrons, the EMCal also registers showers associated with hadrons. Because hadron

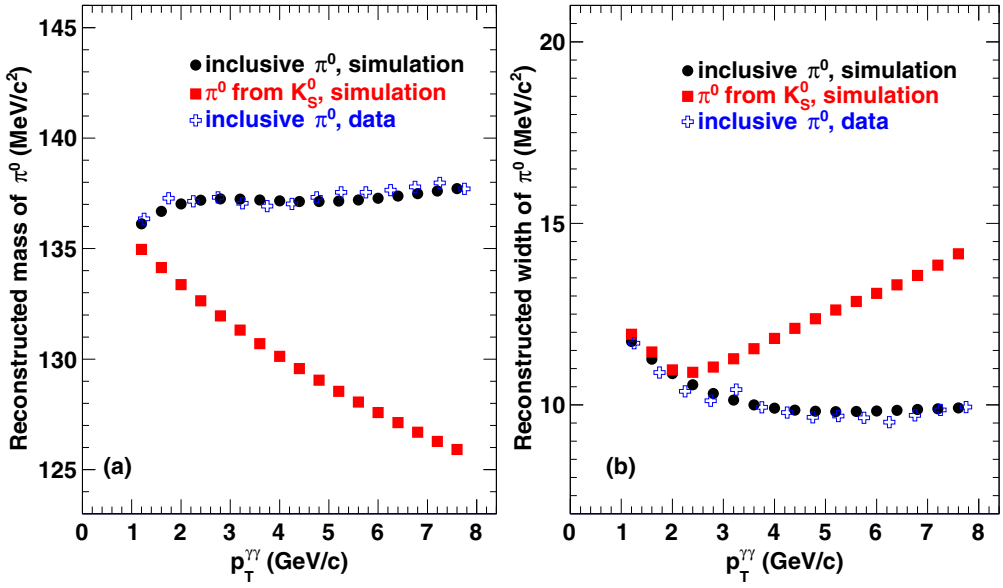

FIG. 1. (Color online) (a) Reconstructed mass and (b) 1σ Gaussian width of π^0 as a function of the reconstructed p_T for inclusive π^0 mesons from data (open crosses), simulations (circles), and for π^0 coming from K^0_S decays (squares) in Cu + Cu collisions.

showers are typically wider than the electromagnetic ones, a shower profile cut [53] is used to reject hadronlike clusters. The shower profile cut is based on a comparison of the registered cluster energy distribution in the EMCal towers to a reference shower shape expected for electromagnetic showers. Most hadrons are not absorbed in the EMCal and traverse it as minimum ionizing particles. The typical hadron energy loss in the EMCal is ~0.3 GeV [53]. To reduce hadron contamination and to account for the poorer EMCal resolution at lower energies, a minimum energy $E_\gamma > 0.2$ GeV is required for clusters reconstructed in all d + Au events and in peripheral Cu + Cu events. In more central Cu + Cu collisions it is increased to $E_\gamma > 0.4$ GeV. The two clusters from the same π^0 meson are also required to fall within the acceptance of the same EMCal sector to suppress boundary effects. The energy balance between the two clusters forming a π^0 candidate is characterized by $\alpha = |E_1 - E_2|/|E_1 + E_2|$, where E_1 and E_2 are the cluster energies. For $\pi^0 \to \gamma\gamma$ decays the parameter α has an almost flat distribution between 0 and 1 [53]. Owing to the steeply falling p_T spectrum of all particles produced in the event, most of the EMCal clusters have a low energy partner; therefore, the distribution of the parameter α calculated for combinatorial pairs has a distinct peak close to 1 for high-p_T pairs. To exclude those pairs, parameter α is required to be less than 0.8.

A pair of γ clusters is selected as a π^0 candidate if its reconstructed invariant mass is within ± 2 standard deviations from a parameterized π^0 mass,

$$|M_{\gamma\gamma}(p_T) - M_{\pi^0}(p_T) \times R_M(p_T)| < 2\sigma_{\pi^0}(p_T) R_\sigma(p_T), \quad (2)$$

where $M_{\gamma\gamma}$ is the reconstructed invariant mass of a pair of the γ clusters, p_T is the transverse momentum of the pair, $M_{\pi^0}(p_T)$ and $\sigma_{\pi^0}(p_T)$ are the parametrizations of the mass, and 1σ width of the π^0 peak as a function of transverse momentum. The parametrization is performed using an inclusive sample of π^0 mesons. $R_M(p_T)$ and $R_\sigma(p_T)$ are correction factors accounting for the difference between inclusive π^0 mesons and neutral pions produced in K^0_S meson decays.

To determine $M_{\pi^0}(p_T)$ and $\sigma_{\pi^0}(p_T)$, the peak position and width of the π^0 peak in the invariant mass distribution of the cluster pairs are measured for different p_T bins and are parameterized as a function of p_T. The mass and width of the π^0 are determined by fitting the invariant mass distribution with a sum of a Gaussian function describing the signal and a second-order polynomial describing the background. Figure 1 shows reconstructed mass and width of the π^0 as a function of p_T in Cu + Cu collisions for one of the EMCal sectors. The uncertainties in the fit parameters, in both data and simulations, are of the order of 1 MeV/c^2 and are not shown in the figure.

Because of the long lifetime of the K^0_S meson, the neutral pions from its decay are produced at a displaced vertex and thus the momentum components of the clusters are misreconstructed. This results in a different reconstructed mass and width of π^0 mesons from K^0_S decays compared to those reconstructed for inclusive π^0 mesons that mostly originate from the event vertex. In the data we have no means to isolate a sample of neutral pions from K^0_S meson decays. Therefore, a quantitative study of this effect is possible only in Monte Carlo simulation. Samples of π^0 mesons produced from the decay of K^0_S mesons with a realistic p_T distribution and neutral pions produced at the primary collision vertex with the inclusive p_T distribution were generated. Neutral pions were reconstructed using the same analysis chain as in real data. From Figs. 1(a) and 1(b), one can see that the reconstructed masses and widths of simulated inclusive π^0 mesons (circles) originating from the event vertex are consistent with the values measured in real data (open crosses). Neutral pions from K^0_S decays are reconstructed with smaller mass and larger width. The correction factors $R_M(p_T)$ and $R_\sigma(p_T)$ are calculated as the ratio of the parameterizations of $M_{\pi^0}(p_T)$ and $\sigma_{\pi^0}(p_T)$ for

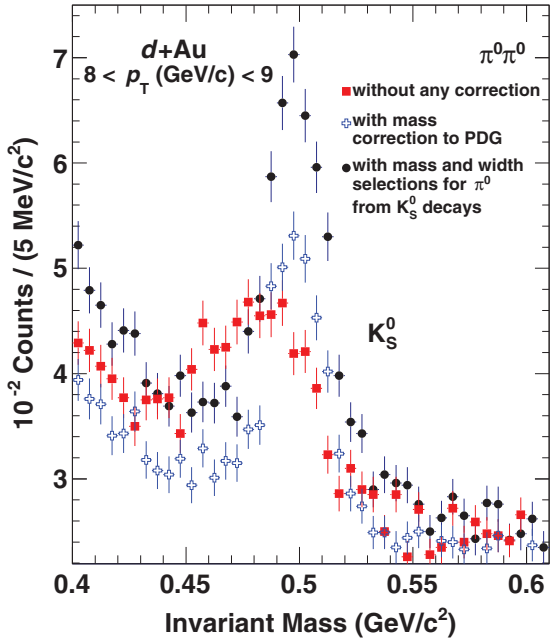

FIG. 2. (Color online) The invariant mass distribution for $\pi^0\pi^0$ pairs measured in the MB d + Au collisions at $8 < p_T < 9$ GeV/c. The invariant mass reconstructed without any corrections is shown with red squares. The invariant mass reconstructed after corrections for the mass of reconstructed π^0 to the PDG value is shown with blue open crosses. Same with additional correction accounting for the difference between inclusive π^0 mesons and neutral pions produced in K^0_S meson decay as described in the text is shown with black circles.

neutral pions from K^0_S mesons and inclusive π^0 mesons. These correction factors improve the signal-to-background ratio by 30%–50%.

The K^0_S mesons are reconstructed by combining the π^0 candidates in pairs within the same event. Pairs of π^0 candidates that share the same cluster are rejected. To improve the signal-to-background ratio π^0, candidates are required to have $p_T > 1.0$ GeV/c in the d + Au sample and $p_T > 1.5$ GeV/c for Cu + Cu events with centrality >20% and $p_T > 2$ GeV/c for Cu + Cu events with centrality <20%.

The red squares in Fig. 2 give an example of the invariant mass distribution for $\pi^0\pi^0$ pairs measured in the MB d + Au collisions at $8 < p_T < 9$ GeV/c. Owing to the steeply falling p_T spectrum of produced particles, the finite energy/position resolution and nonlinear response of the EMCal, the reconstructed mass of π^0 mesons differs from the nominal PDG value $M_{\rm PDG} = 134.98$ MeV [52]. To match the reconstructed mass of π^0 candidates to the PDG value, the energy and momentum of clusters building a pair are multiplied by the ratio of measured and nominal π^0 mass: $M_{\rm PDG}/M_{\gamma\gamma}$. This correction decreases the width of reconstructed K^0_S meson peak by ≈50%. An example of the invariant mass distribution after energy correction is shown with blue open crosses in Fig. 2. The black circles correspond to the case when π^0 candidate selection is changed according to Eq. (2) to account for the difference between inclusive π^0 mesons and neutral pions produced in K^0_S meson decays.

The K^0_S meson raw yield in each p_T bin is extracted by fitting the $\pi^0\pi^0$ invariant mass distribution to a combination of a Gaussian function for the signal and a polynomial for the background. A second-order polynomial provided adequate description of the background shape outside of the K^0_S peak and varied smoothly under the peak. The fitting range was set to about ±8 standard deviations from the peak center and was enough to constrain the fit. A wider fitting range would require a higher order polynomial to describe the background. All fits resulted in χ^2/d.o.f. values close to 1. The K^0_S meson yield in each p_T bin is calculated as the integral of the Gaussian function. Examples of $\pi^0\pi^0$ invariant mass distributions are shown in Figs. 3(a) and 3(b) for d + Au and Cu + Cu, respectively.

The typical signal/background ratio, integrated within $\pm 2\sigma$ around particle mass, for different centrality classes grows from 0.5 to 0.86 (0.04–0.85) in d + Au (Cu + Cu) collisions with increasing transverse momentum. The width and the mass of the reconstructed K^0_S mesons were found to be in good agreement with the values expected from simulation.

B. Reconstruction of K^{*0} meson invariant mass

The K^{*0} and $\overline{K^{*0}}$ mesons are reconstructed from their hadronic decay channels $K^+\pi^-$ and $K^-\pi^+$, respectively. We denote the average of K^{*0} and $\overline{K^{*0}}$ as K^{*0}. Tracks selected for this analysis are required to have $p_T > 0.3$ GeV/c. The TOF system used in this analysis covers approximately one half of the east central-arm spectrometer acceptance and can identify charged kaons up to approximately 2.5 GeV/c [50]. To extend the high-p_T reach of the K^{*0} meson measurement, unidentified, oppositely charged tracks are also included in the analysis. These tracks are required to have associated hits in PC3 or EMCal and are referred to as the PC3-matched tracks. Depending on the track selection criteria, three different techniques are considered in this analysis:

(i) *fully identified*, where tracks are identified as kaons and pions via the TOF;
(ii) *kaon identified*, where one of the tracks is identified as a kaon via the TOF and the other is a PC3-matched track to which the pion mass is assigned;
(iii) *unidentified*, where both tracks are the PC3-matched tracks.

The three techniques are exclusive to each other and statistically independent. The PC3-matched tracks are assigned the nominal mass of the π or K mesons depending on which technique is used. The p_T ranges accessible in the different techniques in p + p, d + Au, and Cu + Cu collisions are given in Table II.

The "fully identified" sample with both charged particles identified in the TOF has the highest signal-to-background ratio and provides access to K^{*0} meson production at low and intermediate p_T. However, owing to the limited PID capabilities of the TOF technique and the small acceptance of the TOF detector, this data set does not provide sufficient statistical precision for $p_T > 4$ GeV/c. The "kaon identified" sample allows for the best signal extraction at intermediate p_T. The "unidentified" sample has a poor signal-to-background

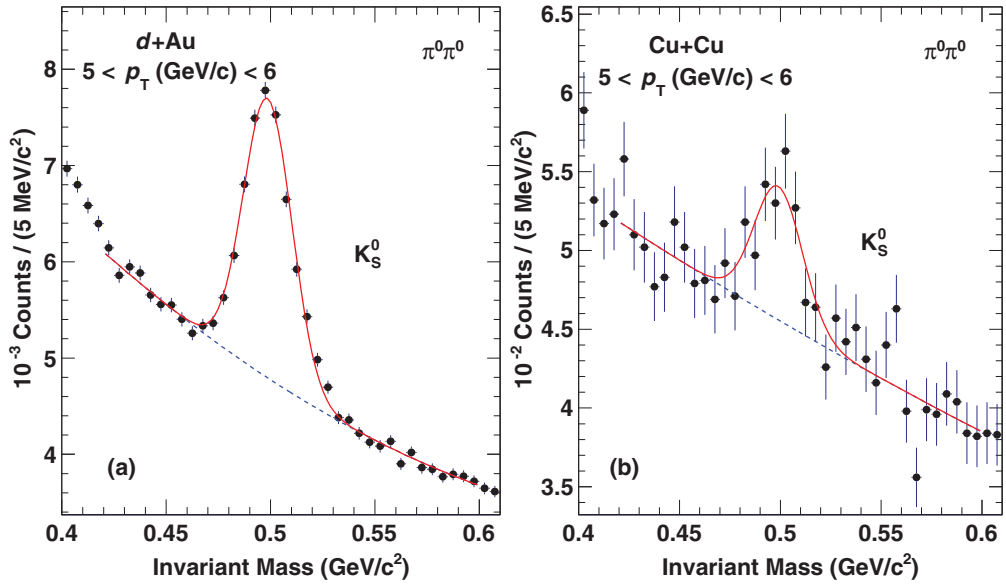

FIG. 3. (Color online) The invariant mass reconstructed from two π^0 mesons in the range $5 < p_T < 6$ GeV/c in (a) $d + \mathrm{Au}$ and (b) $\mathrm{Cu} + \mathrm{Cu}$ collisions at $\sqrt{s_{NN}} = 200$ GeV for the MB data. The distributions are approximated by a Gaussian plus a second-order polynomial shown by solid red and blue dashed curves, respectively.

ratio that prevents signal extraction at low p_T. Signal extraction is possible at higher $p_T > 2.3$ GeV/c in $p + p$ or $d + \mathrm{Au}$ collisions and $p_T > 2.9$ GeV/c in $\mathrm{Cu} + \mathrm{Cu}$ collisions, because of the smaller combinatorial background. The highest p_T reach of K^{*0} measurements with the "unidentified" sample is limited only by the sampled luminosity. Measurements performed with the three techniques have a wide overlap region that is used for evaluation of the systematic uncertainties.

The invariant mass distribution for $K\pi$ pairs comprises both signal and background. The uncorrelated part of the background that arises from the random combination of tracks in the same event is estimated using the mixed-event technique [54]. The event-mixing technique combines positively (negatively) charged tracks from one event with the charged tracks of opposite sign from another event within the same centrality class. The number of mixed events for each event in the data is set to 20 for $p + p$ and $d + \mathrm{Au}$ and to 10 for $\mathrm{Cu} + \mathrm{Cu}$ collisions to have sufficient statistics. The mixed-event invariant mass distribution is normalized by the number of events mixed and then it is subtracted from the unlike-sign distributions. The correlated part of the background is dominated by track pairs from misreconstructed or not fully reconstructed decays of light hadrons. Two such processes, $\phi \to K^+K^-$ and $K^0_S \to \pi^+\pi^-$, produce smeared peak structures in the invariant mass distribution in the close vicinity of the K^{*0} mass peak. Contributions of these two sources are estimated using measured yields of the ϕ meson [15] and K^0_S meson [38]. The location and shape of these peaks are modeled by the PHENIX-based simulations. The estimated contributions are then normalized by the number of events analyzed for K^{*0} meson and subtracted from the measured K^{*0} invariant mass distributions. Apart from these contributions, a residual background owing to other correlated sources [39] remains in the subtracted spectra. The residual background is different depending on the collision systems, analysis techniques, and the pair p_T. Examples of invariant mass distributions for $K\pi$ candidates, where the K is identified in the TOF and the pion mass is given to the PC3 matched tracks, are shown in Figs. 4(a)–4(c) for $p + p$, $d + \mathrm{Au}$, and $\mathrm{Cu} + \mathrm{Cu}$ collisions, respectively. The distributions are shown after subtraction of the mixed-event background and correlated background from $\phi \to K^+K^-$. The contribution from $K^0_S \to \pi^+\pi^-$ is negligible in this case, as K is identified in the TOF. The ϕ contribution is shown by the magenta histogram. It is seen that this contribution is very small in the $\mathrm{Cu} + \mathrm{Cu}$ case, even smaller in the $d + \mathrm{Au}$ case, and negligible in the $p + p$ case. The residual background is clearly seen in the subtracted mass spectra. In the "fully identified technique," this residual background is relatively small. It is larger in the

TABLE II. Different techniques used in K^{*0} measurement and their p_T coverage in $p + p$, $d + \mathrm{Au}$, and $\mathrm{Cu} + \mathrm{Cu}$ collisions at $\sqrt{s_{NN}} = 200$ GeV. The table also shows the range of signal-to-background, integrated within $\pm 3\sigma$ around particle mass (S/B), values for each sample.

Collision system	Technique used	p_T range (GeV/c)	S/B
$p + p$	Fully identified	1.1–4.0	0.011–0.023
	Kaon identified	1.1–4.0	0.005–0.0147
	Unidentified	2.3–8.0	0.006–0.021
$d + \mathrm{Au}$	Fully identified	1.1–4.0	0.009–0.015
	Kaon identified	1.4–4.5	0.003–0.0118
	Unidentified	2.3–8.5	0.009–0.012
$\mathrm{Cu} + \mathrm{Cu}$	Fully identified	1.4–4.0	0.0048–0.0076
	Kaon identified	1.7–4.5	0.0006–0.0039
	Unidentified	2.9–8.0	0.0011–0.0036

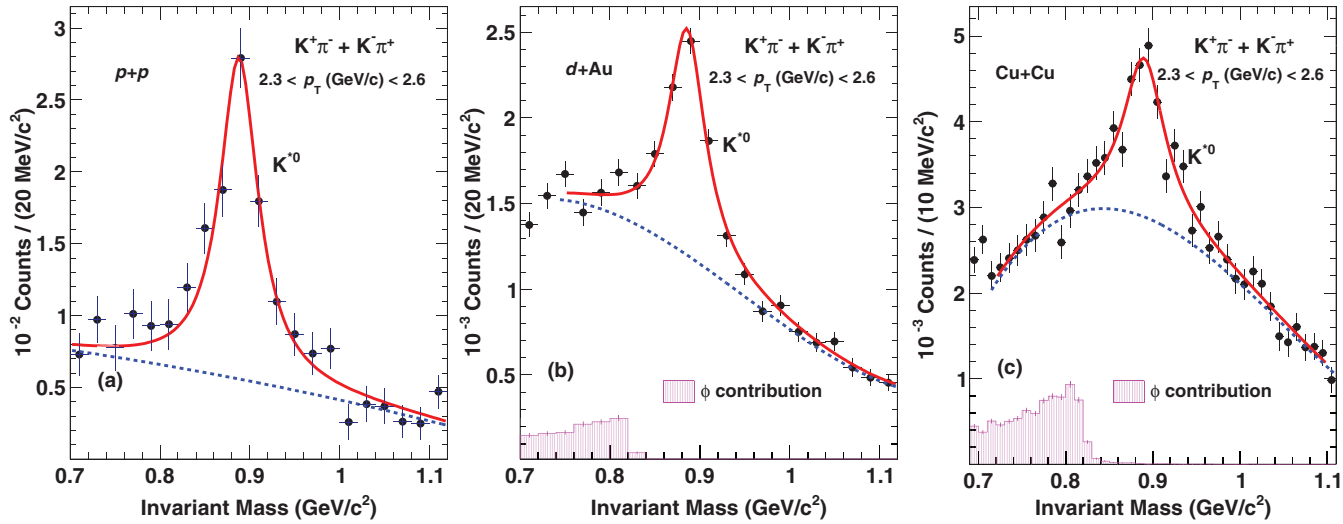

FIG. 4. (Color online) The invariant mass distributions of $K\pi$ candidates, where K is identified in the TOF and π is matched in PC3, in the range $2.3 < p_T < 2.6$ GeV/c for (a) $p+p$, (b) $d+$Au, and (c) Cu + Cu collisions at $\sqrt{s_{NN}} = 200$ GeV. The distributions are shown after subtraction of the mixed-event background and the correlated background from misidentified $\phi \to K^+K^-$ decays (see text for details). The distributions are fitted to the sum of the RBW function for the signal and a polynomial (second order in $p+p$ and third elsewhere) for the background shown with a solid red curve. The residual background is also shown separately with a blue dashed curve. The ϕ contribution is shown by the magenta histogram.

"kaon-identified technique" and even larger in the analysis based on unidentified tracks.

The invariant mass distribution in each p_T bin is fit to the sum of a relativistic Breit-Wigner (RBW) function for the signal and a second- or third-order polynomial for the residual background,

$$\mathrm{RBW} = \frac{1}{2\pi}\frac{M_{K\pi}M_{K^{*0}}\Gamma}{\left(M^2_{K\pi}-M^2_{K^{*0}}\right)^2+M^2_{K^{*0}}\Gamma^2}, \tag{3}$$

where $M_{K\pi}$ is the reconstructed invariant mass, $M_{K^{*0}}$ is the fitted mass of the K^{*0} meson, and Γ is the width of the K^{*0} meson fixed to the value obtained from simulation. Because the experimental mass resolution ($\sim$5 MeV/c^2) is much smaller than the natural width of the K^{*0} meson, the simulated Γ is very close to the nominal width of 48.7 MeV/c^2 [52].

Owing to the difference in the shape of the invariant mass distributions of K^0_S and K^{*0} mesons, two different methods are used to obtain their raw yields. The reconstructed K^0_S meson peak in the invariant mass distribution has a Gaussian shape with a width of $\sim$12–14 MeV/c^2, whereas the K^{*0} meson peak has much wider width ($\sim$48 MeV/c^2) and long tails intrinsic to RBW distribution. Hence, it is convenient to use the Gaussian integral to obtain the raw yield for K^0_S meson owing to its well-defined shape. To obtain the raw yield for K^{*0} meson, it is sensible to use bin counting in a limited mass window. In the present analysis we used a mass window of $\pm$75 MeV/c^2, around the nominal mass of K^{*0} meson, which includes both signal and residual background. The residual background contribution is obtained by integrating the background component of the fit (second- or third-order polynomial) in the same mass window and subtracted from the total signal to obtain the raw yield for K^{*0} meson. It is important to note that both the integration and the bin counting methods are used to estimate the systematic uncertainties in the K^0_S and K^{*0} meson yields (see Sec. III D).

C. Calculation of invariant yields

The invariant yields of K^0_S and K^{*0} mesons are calculated by

$$\frac{1}{2\pi p_T}\frac{d^2N}{dp_T dy} = \frac{1}{2\pi p_T\,\Delta p_T\,\Delta y} \times \frac{Y_{\mathrm{raw}}}{N_{\mathrm{evt}}\,\epsilon(p_T)\,\mathrm{BR}} \times \frac{C_{\mathrm{bias}}}{\epsilon_{\mathrm{treff}}}, \tag{4}$$

where Y_{raw} is the meson raw yield (see Secs. III A and III B), N_{evt} is the number of sampled events in the centrality bin, and $\epsilon(p_T)$ includes geometrical acceptance, reconstruction efficiency, and occupancy effects in the high-multiplicity environment of heavy-ion collisions. The branching ratio (BR) for $K^0_S \to \pi^0\pi^0$ is 30.69 $\pm$ 0.05% (BR for $\pi^0 \to 2\gamma$ is 98.823 $\pm$ 0.034%). The branching ratio for the $K^{*0} \to K^+\pi^-$ is close to 67%. The trigger bias correction C_{bias} is 0.69 [15] for $p+p$ collisions and for $d+$Au collisions it varies from 1.03 to 0.94 [29] with increasing centrality. The trigger bias correction in the Cu + Cu collision system is taken equal to unity in all analyzed centrality bins. The ERT efficiency for K^0_S meson $\epsilon_{\mathrm{treff}}$ determines the probability of $K^0_S \to \pi^0\pi^0 \to 4\gamma$ decay products to fire the ERT. For the K^{*0}, which uses no additional trigger, $\epsilon_{\mathrm{treff}} = 1$.

The invariant cross section in the $p+p$ system is given by

$$E\frac{d^3\sigma}{dp^3} = \sigma^{\mathrm{inel}}_{pp} \times \frac{1}{2\pi\,p_T}\frac{d^2N}{d\,p_T dy}, \tag{5}$$

where $\sigma^{\mathrm{inel}}_{pp} = 42.2 \pm 3$ mb [38] is the total inelastic cross section in $p+p$ collisions at $\sqrt{s} = 200$ GeV.

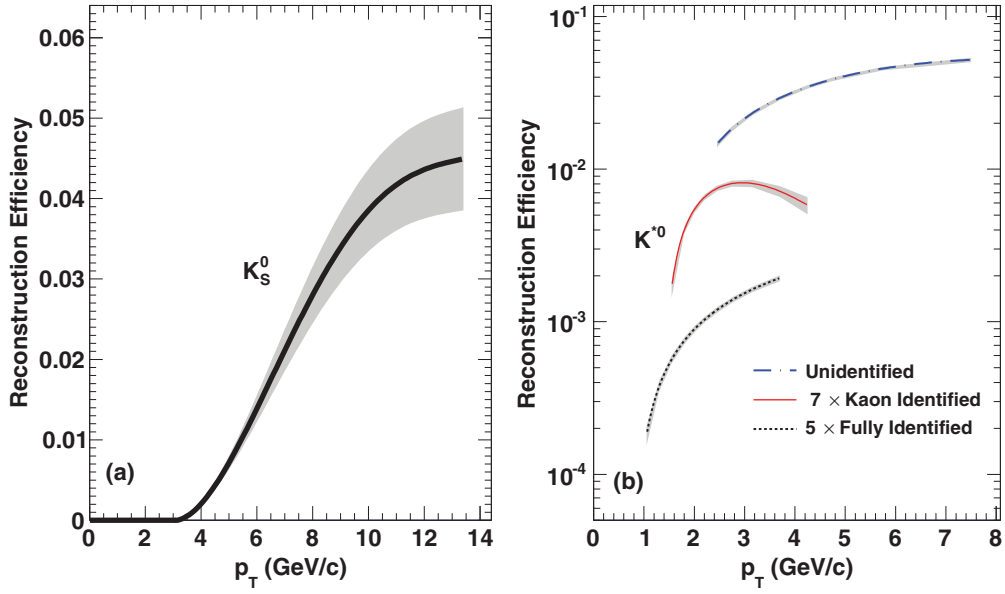

FIG. 5. (Color online) Reconstruction efficiency for (a) K^0_S and (b) K^{*0} for $d+$Au collisions. The gray bands show the systematic uncertainty. Please refer to Table III for systematic uncertainties. Panel (b) shows the reconstruction efficiencies for the "unidentified," "kaon identified," and "fully identified" techniques for the K^{*0} analysis are shown by the dot-dashed blue curve, red solid curve, and black dashed curve, respectively.

The reconstruction efficiencies for the K^0_S and K^{*0} mesons are obtained from Monte Carlo simulations. Both the K^0_S and the K^{*0} mesons are generated using the single-particle event generator EXODUS [55]. The primary mesons are decayed into the measured channel and all particles are traced through the PHENIX setup using the GEANT [56]-based PHENIX simulation package. The decayed particles are reconstructed using the same analysis procedures used in the analysis of real data. The reconstruction efficiency is calculated as the ratio of the number of reconstructed mesons counted in the same way as in data to the number of generated mesons and is found to be the same for $p+p$ and $d+$Au collision systems. Owing to high detector occupancy in Cu + Cu collisions, the reconstruction efficiency becomes smaller owing to hit and cluster merging in the detector subsystems. To take this effect into account the reconstruction efficiencies for K^0_S and K^{*0} mesons were determined after embedding the simulated signals in real events. The K^{*0} meson reconstruction efficiency in Cu + Cu is reduced by ∼5% in the most central collisions and by ∼1% in peripheral collisions. These corrections are included in $\epsilon(p_T)$, as shown in Fig. 5.

The probability that one of the K^0_S meson decay products fires the ERT trigger is estimated based on the measured single-photon ERT efficiency, ϵ_γ. The latter is evaluated as the ratio of the number of clusters that fired the ERT to the number of clusters of the same energy in the MB data sample. The trigger efficiency is calculated as a function of cluster energy separately for each EMCal sector. An example of ϵ_γ in one of the EMCal sectors is shown in Fig. 6(a) for the case of Cu + Cu collisions.

The trigger efficiency grows steeply with energy and reaches 50% at the energy approximately corresponding to the ERT threshold setting. The curves saturate at approximately twice the threshold energy. The level of saturation is below 100% because of inactive areas of the ERT. The trigger efficiency for K^0_S meson (ϵ_{treff}) is evaluated using Monte Carlo simulations. The K^0_S meson is considered to fire the ERT if at least one of the photons in the final state fires the trigger. The resulting trigger efficiency for $K^0_S \to \pi^0(\to \gamma\gamma)\pi^0(\to \gamma\gamma)$ is shown in Fig. 6(b). The trigger efficiency uncertainty for K^0_S mesons was evaluated by varying the single-photon ERT efficiency within the uncertainties of the measurement.

D. Systematic uncertainties

1. *Systematic uncertainties for* K^0_S

Several factors contribute to the systematic uncertainty of the measurement of the K^0_S meson invariant yield: the raw yield extraction, the reconstruction efficiency and detector acceptance, and the $K^0_S \to \pi^0\pi^0$ decay branching ratio uncertainty. Evaluation of the systematic uncertainties associated with the K^0_S meson raw yield extraction is done by varying the raw yield extraction method and by modifying the background shape around the K^0_S peak. The $\pi^0\pi^0$ invariant mass distribution is approximated by a second-order polynomial outside three standard deviations from the center of the peak region. The polynomial is then interpolated under the peak and subtracted from it. The yield is obtained by integrating the subtracted invariant mass distribution in a three-standard-deviation window around the mean of the peak. To modify the background shape, the "cross π^0 meson" cut is used. This cut significantly changes the background shape in the invariant mass distributions of $\pi^0\pi^0$ pairs in the vicinity of the K^0_S meson peak. If two photons with the largest energy, assigned to different π^0 candidates, produce an invariant mass within $\pm 4 \times \sigma_{\pi_0}(p_T)$ from the $M_{\pi^0}(p_T)$ given in Eq. (2), the

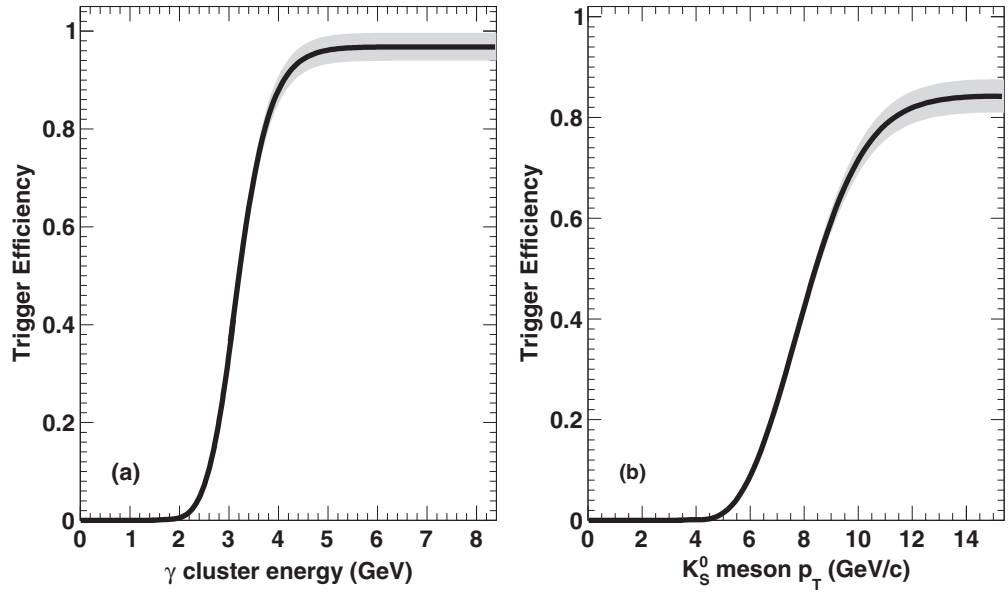

FIG. 6. (a) Trigger efficiency for single photons as a function of cluster energy. (b) K^0_S trigger efficiency as a function of p_T. The bands show the systematic uncertainty. Results are presented for the Cu + Cu data recorded in 2005.

entire combination of four clusters is rejected. The rms of the corrected raw yields obtained in all combinations of yield extraction and background modification is taken as an estimate of the systematic uncertainty for the signal extraction.

The uncertainty in the reconstruction efficiency is dominated by mismatches in detector performance between data and Monte Carlo. The uncertainty on the EMCal acceptance is estimated by artificially increasing dead areas in the EMCal by 10% and redoing the analysis. To estimate the contribution of the EMCal energy resolution to the systematic uncertainty, the K^0_S meson reconstruction efficiency is recalculated with the energy resolution artificially worsened by 3%. The 3% variation of the energy resolution was chosen as a maximum value that would still provide consistency between the π^0 meson widths from real data and simulations. The contribution of the EMCal energy scale uncertainty was estimated by varying the energy scale within $\pm 1\%$ in simulation. The variation range is constrained by the π^0 meson peak positions in real data and simulation. Photon conversion in the detector material is accounted for in the calculation of the reconstruction efficiency. However, detector materials are described in the simulation with some precision and thus an uncertainty associated with the photon conversion is introduced. The conversion correction uncertainty was estimated in Ref. [53] to be equal to 3% for the neutral pions. Thus, the K^0_S meson conversion correction uncertainty is 6%.

The π^0 meson candidates are selected within two standard deviations around the π^0 meson peak position in the invariant mass distribution of two photons. The difference between the π^0 meson width parametrizations in real data and Monte Carlo simulations does not exceed 10%. To estimate the π^0 selection cut uncertainty, the window around the π^0 meson peak position is varied by 10%. The difference between the K^0_S meson reconstruction efficiencies calculated with changed and default cuts is taken as the uncertainty related to the π^0 candidate selection cut. The K^0_S meson trigger efficiency uncertainty is evaluated by varying the single photon ϵ_γ trigger efficiency within the uncertainties of its measurement. Relative systematic uncertainties for the K^0_S meson measurements in $d+\mathrm{Au}$ and $\mathrm{Cu}+\mathrm{Cu}$ systems are given in Table III. The uncertainties are categorized by types: A, B, and C. Type A denotes the p_T uncorrelated uncertainty, type B denotes the p_T correlated uncertainty, and type C denotes the overall normalization uncertainty such as the MB trigger efficiency in $p+p$ and $d+\mathrm{Au}$ collisions, branching ratio of the parent particle, γ-conversion factor, etc.

2. *Systematic uncertainties for K^{*0}*

The main systematic uncertainties of the K^{*0} measurement include uncertainties in the raw yield extraction, EMCal-PC3 matching, TOF PID cuts, track momentum reconstruction,

TABLE III. Relative systematic uncertainties in percent for the K^0_S meson measurement. The given ranges indicate the variation of the systematic uncertainty over the p_T range of the measurement.

Source	$d+\mathrm{Au}$ (%)	$\mathrm{Cu}+\mathrm{Cu}$ (%)	Uncertainty type
Raw yield extraction	4–31	14–26	A
Acceptance	6	5	B
ERT efficiency	2–7	3–4	B
EMCal energy resolution	4–5	3–6	B
EMCal scale	4–5	3–5	B
π^0 selection	5–11	6–10	B
γ conversion	6	6	C
Branching ratio	0.2	0.2	C
BBC cross section	8	–	C

TABLE IV. Relative systematic uncertainties in percent for the K^{*0} meson measurement in "kaon identified" technique. The given ranges indicate the variation of the systematic uncertainty over the p_T range of the measurement.

Source	$p+p$ (%)	$d+$Au (MB) (%)	Cu + Cu (MB) (%)	Uncertainty type
Raw yield extraction	5–8	7–12	2–4	A
Acceptance	1–5	3–7	1–3	B
Track momentum reconstruction	1–4	2–7	1–5	B
Track matching	1–4	4–7	2–13	B
TOF PID	1–6	4–9	1–4	B
BBC cross section	10	8	–	C

acceptance, and BBC cross section. The systematic uncertainty associated with the raw yield extraction is estimated by varying the fitting ranges, varying the width of the K^{*0} meson peak by $\pm 2\%$ around its simulated value and taking the integral of the fitted RBW function instead of summing up the yield in each p_T bin. In addition, the yield difference when the K^{*0} meson mass is fixed to the PDG value and when it is a free parameter in the fit of the mass spectrum is included in the systematic uncertainty. To evaluate the uncertainties from EMCal-PC3 matching and TOF PID cuts, the corresponding cuts are varied within $\pm 17\%$. The uncertainty in momentum reconstruction is estimated by varying the momentum scale within 0.5% in the simulation. The systematic uncertainties for all three techniques in a particular collision system are similar. A summary of the systematic uncertainties for the case of "kaon identified" analysis technique in $p+p$, $d+$Au, and Cu + Cu collisions is given in Table IV.

IV. RESULTS AND DISCUSSIONS

In this section we present p_T spectra of K^0_S and K^{*0} mesons in $p+p$, $d+$Au, and Cu + Cu collisions at $\sqrt{s_{NN}} = 200$ GeV. The invariant p_T spectra are used to calculate the nuclear modification factors in $d+$Au and Cu + Cu collisions at different centralities. These nuclear modification factors are compared to those previously measured for neutral pions, charged kaons, ϕ mesons, and protons.

A. Invariant transverse momentum spectra

Figure 7(a) shows the cross section of K^{*0} meson production as a function of p_T in $p+p$ collisions at $\sqrt{s} =$ 200 GeV. Experimental points shown with different symbols correspond to the different analysis techniques listed in Table II. The systematic uncertainties, mostly uncorrelated for different techniques, are shown along with the data points and include raw yield extraction, track matching, and TOF PID uncertainties listed in Table IV.

The solid line in Fig. 7(a) is the result of a common fit of the data with the Tsallis function in the form used in

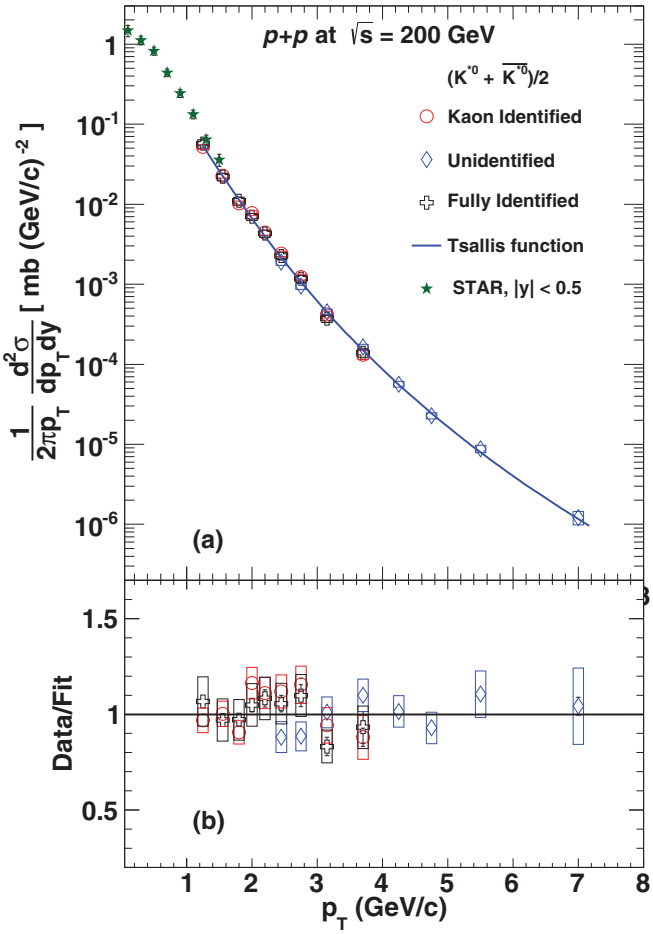

FIG. 7. (Color online) (a) Cross section of K^{*0} meson production as a function of p_T obtained with the "kaon identified," "fully identified," and "unidentified" analysis techniques in $p+p$ collisions at $\sqrt{s} = 200$ GeV. The systematic uncertainties shown with boxes are mostly uncorrelated between analysis techniques. The solid blue line is the Tsallis function fit to the combined data points. The star symbols are the K^{*0} meson measurements from the STAR Collaboration [39]. (b) Ratio of the yields obtained with the three analysis techniques to the fit function. The scale uncertainty of 10% is not shown.

Ref. [38],

$$\frac{1}{2\pi}\frac{d^2\sigma}{dydp_T} = \frac{1}{2\pi}\frac{d\sigma}{dy}\frac{(n-1)(n-2)}{[nT+m(n-1)](nT+m)} \times \left(\frac{nT+m_T}{nT+m}\right)^{-n}, \quad (6)$$

where $d\sigma/dy$, n, and T are the free parameters, $m_T = \sqrt{{p_T}^2+m^2}$, and m is the mass of the particle of interest. The parameter T determines the shape of the spectrum at low p_T, where particle production is dominated by soft processes, whereas n governs the high-p_T part of the spectrum dominated by particles produced in hard scattering. The fit parameters to the $p+p$ data are $d\sigma/dy = 1.28 \pm 0.14$ mb, $T = 121 \pm 19$ (MeV), and $n = 9.67 \pm 0.62$, with $\chi^2/\text{d.o.f.} = 6.9/10$. The uncertainties in the parameters include both the statistical and the systematic uncertainties in quadrature.

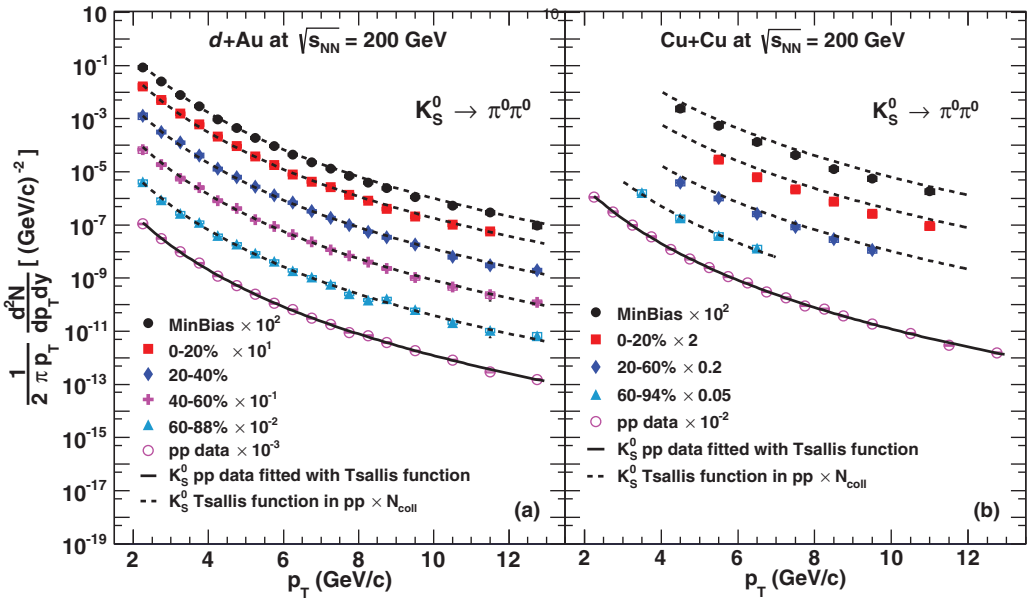

FIG. 8. (Color online) K^0_S meson invariant p_T spectra (a) for $d+$Au and (b) for Cu + Cu collisions at $\sqrt{s_{NN}} = 200$ GeV for different centrality bins. The systematic uncertainties are shown by the boxes. The solid curves are a fit of the K^0_S $p+p$ data by the Tsallis function [38]. The dashed curves are the fit function scaled by $N_{\rm coll}$. The global $p+p$ uncertainty of ~10% is not shown.

Figure 7(b) shows the ratio of the K^{*0} meson cross sections obtained with the different techniques to the fit. A good agreement is observed for the cross sections obtained with different analysis techniques, demonstrating the robustness of the results. The final K^{*0} production spectrum is obtained by standard weighted averaging [52] of the cross sections and uncorrelated errors for the same p_T bin obtained from the different analysis techniques. The STAR experiment measured the K^{*0} over the p_T range 0–1.5 GeV/c, shown by the solid star symbols in Fig. 7(a). In the overlap region STAR results agree with our measurement within 1σ of combined statistical and systematic uncertainties.

Figures 8 and 9 show the invariant p_T spectra of K^0_S and K^{*0} mesons in $d+$Au and Cu + Cu collisions, respectively, at $\sqrt{s_{NN}} = 200$ GeV. The results for different centrality bins are scaled by arbitrary factors for clarity. The $p+p$ results for K^0_S, both the data points and the parameters of the Tsallis fit, are taken from Ref. [38]. The published cross section of K^0_S meson production and the cross section of the K^{*0} meson production, shown in Fig. 7, are converted into yield using

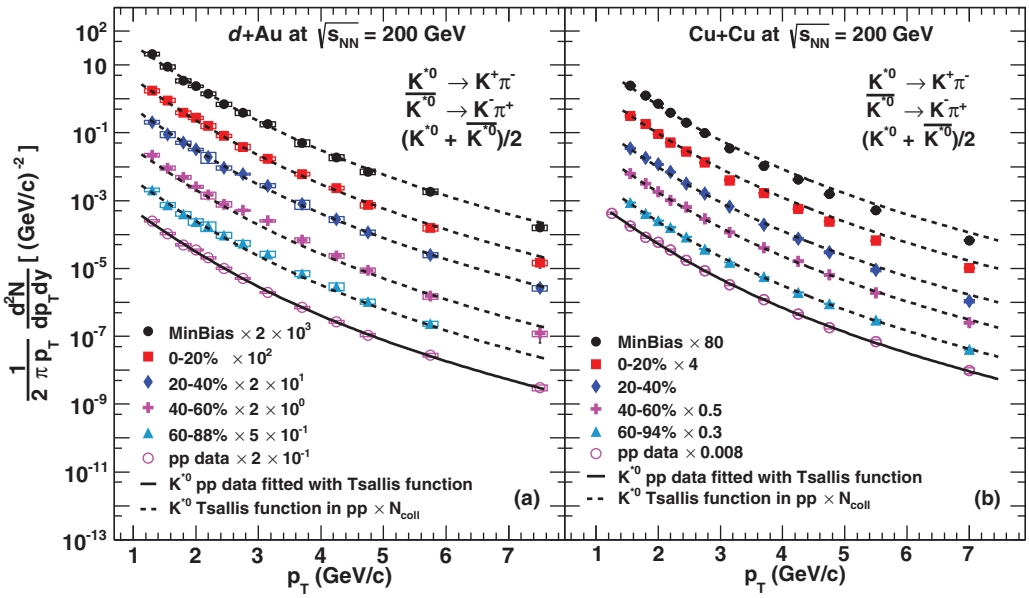

FIG. 9. (Color online) K^{*0} meson invariant p_T spectra (a) for $d+$Au and (b) for Cu + Cu collisions at $\sqrt{s_{NN}} = 200$ GeV for different centrality bins. The systematic uncertainties are shown by the boxes. The solid curve is a fit of the K^{*0} $p+p$ data by the Tsallis function [38]. The dashed curves are the fit function scaled by $N_{\rm coll}$. The global $p+p$ uncertainty of ~10% is not shown.

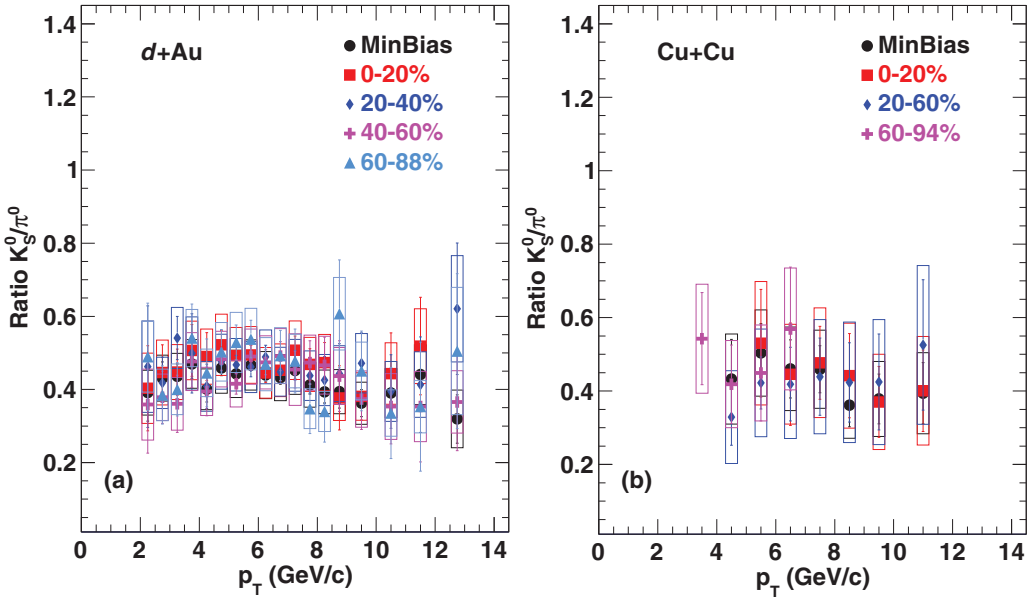

FIG. 10. (Color online) K^0_S/π^0 ratios for (a) $d+$Au and (b) Cu + Cu collisions at $\sqrt{s_{NN}} = 200$ GeV for different centrality bins. The statistical uncertainties are shown by vertical bars and the systematic uncertainties are shown by the boxes.

Eq. (5) and shown with open circles in Figs. 8 and 9. The solid curves represent the Tsallis fit to the $p+p$ data. The dashed curves represent the same fit, scaled by the number of binary collisions corresponding to the centrality bins concerned. In $d+$Au collisions, the production of both mesons follows the binary scaling for all centralities in the measured p_T range. A similar behavior is also observed in peripheral Cu + Cu collisions. In central and semicentral Cu + Cu interactions, the production of K^0_S and K^{*0} mesons is suppressed at $p_T >$ 4 GeV/c and $p_T >$ 2–3 GeV/c, respectively.

Figure 10 shows the ratio K^0_S/π^0 for different centrality bins in Cu + Cu collisions at $\sqrt{s_{NN}} = 200$ GeV. The ratio is flat with respect to p_T with a value of ∼0.5, irrespective of the system and collision centrality. The statistical uncertainties are shown by vertical bars and the systematic uncertainties are shown by boxes.

B. Nuclear modification factors

The nuclear modification factors for K^0_S and K^{*0} mesons were calculated using Eq. (1). The average number of inelastic nucleon-nucleon collisions $\langle N_{\rm coll}\rangle$ and participants $\langle N_{\rm part}\rangle$ estimated for each centrality bin analyzed in $d+$Au and Cu + Cu collisions are summarized in Table V [57,58].

Figure 11 shows the nuclear modification factors $R_{d\rm Au}$, measured for the K^0_S and K^{*0} mesons in the most central and peripheral $d+$Au collisions at $\sqrt{s_{NN}} = 200$ GeV. Within uncertainties, the $R_{d\rm Au}$ are consistent with unity for all centralities at $p_T >$ 1 GeV/c. However, in the most central $d+$Au collisions, there is a hint of a modest Cronin-like enhancement in the range $2 < p_T < 5$ GeV/c and of suppression at $p_T >$ 6–8 GeV/c. Results for ϕ and π^0 mesons [15,59] and protons [29] are also shown for comparison in Fig. 11. The $R_{d\rm Au}$ for all measured mesons shows similar behavior. Based on these results one can conclude that either the cold-nuclear-matter (CNM) effects do not play an important role in the production of these mesons or different CNM effects compensate each other in the studied p_T range. Unlike mesons, baryons [29] exhibit a strong enhancement at intermediate transverse momenta in (semi)central $d+$Au collisions that could be explained by recombination models [33].

Figure 12 shows the nuclear modification factors $R_{\rm CuCu}$ measured for K^0_S and K^{*0} mesons in Cu + Cu collisions at $\sqrt{s_{NN}} = 200$ GeV. The results are presented for different centrality bins corresponding to the $\langle N_{\rm coll}\rangle$ and $\langle N_{\rm part}\rangle$ given in Table V. In peripheral Cu + Cu collisions the production of K^0_S and K^{*0} mesons follows the binary scaling as expected from Figs. 8 and 9. The $R_{\rm CuCu}$ factors become smaller with increasing centrality and in the most central Cu + Cu collisions the production of both mesons is suppressed at high p_T. For the most central collisions, $R_{\rm CuCu}$ drops to a value of 0.5 at $p_T >$ 5 GeV/c, both for K^0_S and K^{*0} mesons.

TABLE V. $N_{\rm coll}$ and $N_{\rm part}$ in $d+$Au and Cu + Cu collisions at $\sqrt{s_{NN}} = 200$ GeV.

Collisions	Centrality bin (%)	$\langle N_{\rm coll}\rangle$	$\langle N_{\rm part}\rangle$
$d+$Au	0–20	15.1 ± 1.0	15.3 ± 0.8
	20–40	10.2 ± 0.7	11.1 ± 0.6
	40–60	6.6 ± 0.4	7.8 ± 0.4
	60–88	3.1 ± 0.2	4.3 ± 0.2
	0–100	7.6 ± 0.4	8.5 ± 0.4
Cu + Cu	0–20	151.8 ± 17.1	85.9 ± 2.3
	20–40	61.6 ± 6.6	45.2 ± 1.7
	40-60	22.3 ± 2.9	21.2 ± 1.4
	60–94	5.1 ± 0.7	6.4 ± 0.4
	0–94	51.8 ± 5.6	34.6 ± 1.2
	20–60	42.0 ± 4.8	33.2 ± 1.6

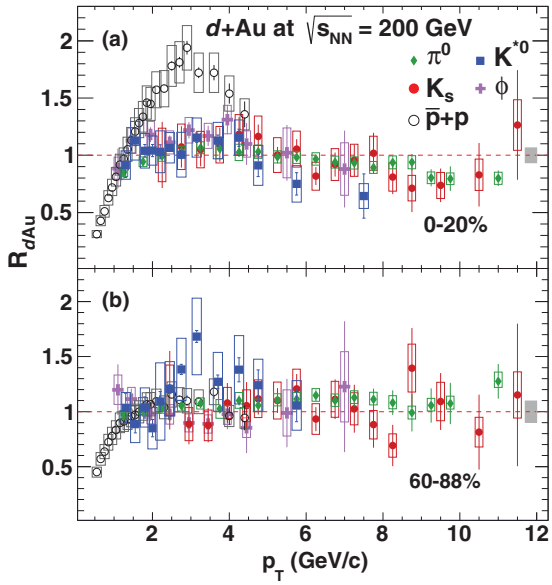

FIG. 11. (Color online) Nuclear modification factor as a function of p_T for K^0_S and K^{*0} for (a) most central and (b) most peripheral $d+$Au collisions at $\sqrt{s_{NN}} = 200$ GeV. Results from π^0 [59], ϕ [15], and protons [29] are also shown. The π^0 results are shown from the data collected in 2003 and the results of the rest of the particles are obtained from 2008 data. The corresponding systematic uncertainties are shown by boxes. The global $p+p$ uncertainty of ~10% is not shown.

Figure 13 compares the R_{CuCu} results for K^0_S and K^{*0} mesons to results obtained for the π^0 meson [8] and the ϕ meson [15] in the most central, most peripheral, and MB Cu + Cu collisions. In peripheral collisions, the nuclear modification factors are consistent with unity for all measured mesons at all p_T. In central and MB collisions, above $p_T \geqslant 5$ GeV/c, the R_{CuCu} of all mesons is below unity, and within the uncertainties the suppression is the same for all measured mesons, indicating that its mechanism does not depend on the particle species. However, at lower p_T between 1 and 5 GeV/c, there are differences among the different particles. The K^{*0} meson R_{CuCu} shows no suppression at $p_T \sim 1$–2 GeV/c and then decreases with increasing p_T, as previously observed for the ϕ meson. The π^0 meson R_{CuCu} shows significantly stronger suppression and flat behavior over the same p_T range.

Figure 14 compares the suppression patterns of light-quark mesons, strange mesons, and baryons. Shown are the R_{AA} of π^0, K^{*0}, and ϕ mesons measured in Cu + Cu at $\sqrt{s_{NN}} =$ 200 GeV. Because there are no measurements of R_{AA} for protons and charged kaons in the Cu + Cu system, we compare to proton and charged kaon measurements made in Au + Au collisions at the same energy [29]. The comparisons are made for centrality bins corresponding to a similar number of participating nucleons (N_{part}), in the Cu + Cu and Au + Au systems: Cu + Cu 40%–94% ($\langle N_{\mathrm{part}}\rangle = 11.93 \pm 0.63$) and Au + Au 60%–92% ($\langle N_{\mathrm{part}}\rangle = 14.5 \pm 2.5$) in the bottom panel and Cu + Cu 0%–40% ($\langle N_{\mathrm{part}}\rangle = 65.5 \pm 2.0$) and Au + Au 40%–60% ($\langle N_{\mathrm{part}}\rangle = 59.95 \pm 3.5$) in the top panel. In peripheral

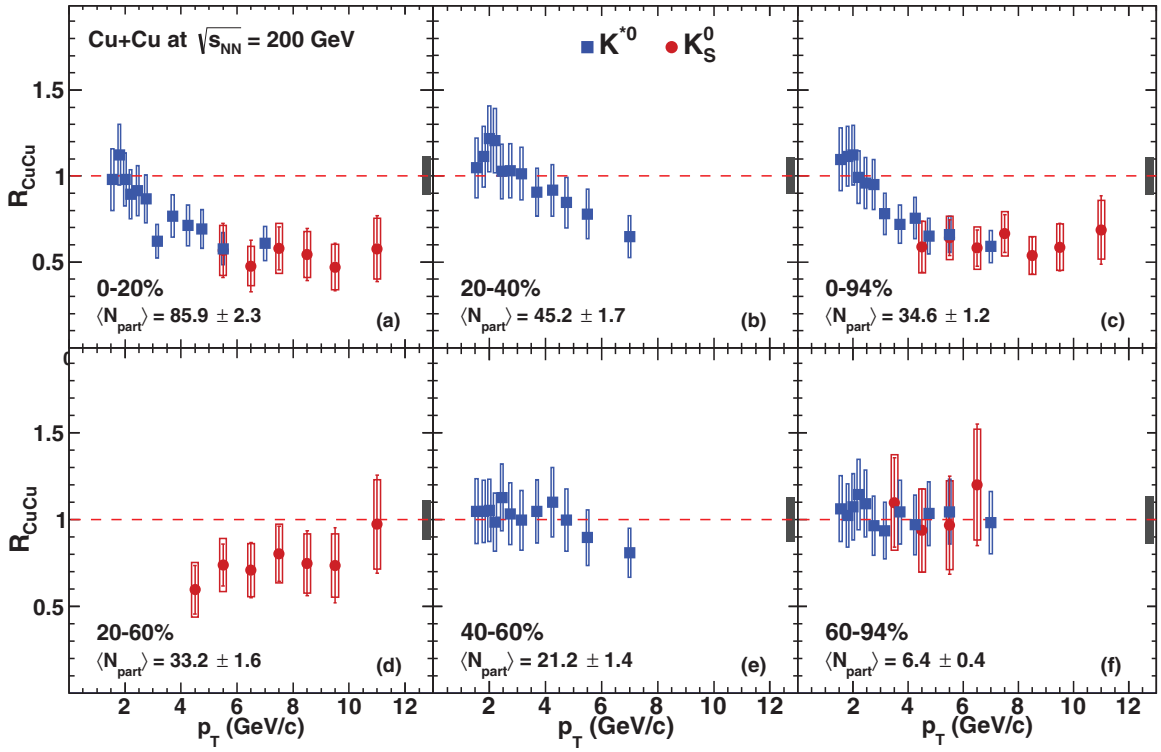

FIG. 12. (Color online) The nuclear modification factor as a function of p_T for K^0_S and K^{*0} meson for centrality bins (a) 0%–20%, (b) 20%–40%, (c) 0%–94%, (d) 20%–60%, (e) 40%–60%, and (f) 60%–94% in Cu + Cu collisions at $\sqrt{s_{NN}} = 200$ GeV. In all panels the statistical uncertainties are shown with vertical bars and the systematic uncertainties are shown with boxes. The global $p+p$ uncertainty of ~10% is not shown.

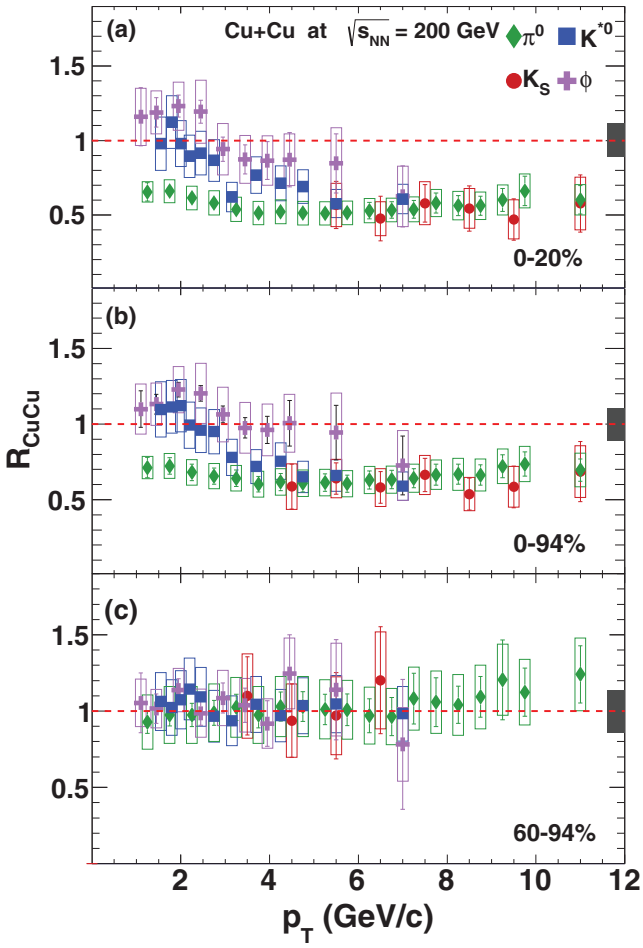

FIG. 13. (Color online) Nuclear modification factor as a function of p_T for K^0_S, K^{*0} for centralities (a) 0%–20%, (b) 0%–94% (MB), and (c) 60%–94% in Cu + Cu collisions at $\sqrt{s_{NN}} = 200$ GeV. Results from π^0 [8] and ϕ [15] are also shown. The statistical errors are shown by vertical bars. The systematic uncertainties are shown by boxes. The global $p + p$ uncertainty of ∼10% is not shown.

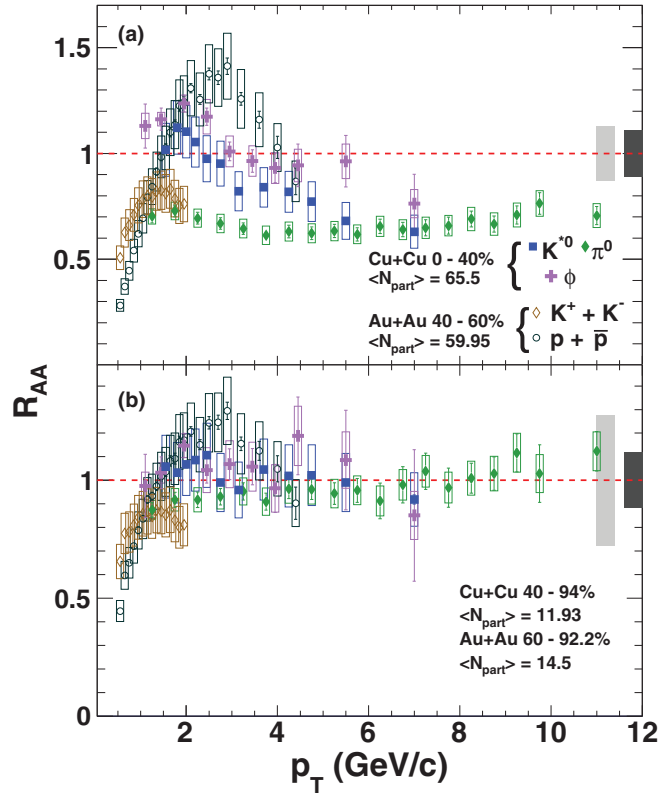

FIG. 14. (Color online) Comparison of the nuclear modification factor of π^0 [8], ϕ [15], and K^{*0} in Cu + Cu collisions and proton [29] and kaon [29] in Au + Au collisions at $\sqrt{s_{NN}} = 200$ GeV. The comparisons are made for (a) 40%–60% and (b) 60%–92% in Au + Au system and 0%–40% and 40%–94% in the Cu + Cu system corresponding to similar $N_{\rm part}$ values in the two systems. The statistical errors are shown by vertical bars. The systematic uncertainties are shown by boxes. The global $p + p$ uncertainty of ∼10% is not shown.

collisions the R_{AA} factors for all mesons are consistent with unity for $p_T > 2$ GeV/c. A modest enhancement of ≈1.3 is observed for protons. In central collisions, all hadrons show suppression. In the intermediate-p_T range ($p_T = 2$–5 GeV/c), there seems to be some hierarchy, with baryons being enhanced, neutral pions being suppressed the most, and K^{*0} and ϕ mesons showing an intermediate behavior. At higher p_T, all particles are suppressed and they seem to reach the same level of suppression, within uncertainties, irrespective of their mass or quark content. The fact that R_{AA} of all mesons becomes the same is consistent with the assumption that energy loss occurs at the parton level and the scattered partons fragment in the vacuum. We also note that the R_{AA} of the K^{*0} and ϕ mesons appear to be very similar to the R_{AA} of electrons from the semileptonic decay of heavy flavor mesons [27]. The present results provide additional constraints to the models attempting to quantitatively reproduce the nuclear modification factors in terms of energy loss of partons inside the medium.

V. SUMMARY AND CONCLUSIONS

The PHENIX experiment measured K^0_S and K^{*0} meson production via $\pi^0\pi^0$ and $K^{\pm}\pi^{\mp}$ decay, respectively, in $p + p$, $d + $Au, and Cu + Cu collisions at $\sqrt{s_{NN}} = 200$ GeV. The invariant transverse momentum spectra and nuclear modification factors are presented for different centralities in the $d + $Au and Cu + Cu systems covering the p_T range of 1.1–8.5 GeV/c and 3–13 GeV/c for K^{*0} and K^0_S, respectively. In the $d + $Au system, the nuclear modification factor of K^0_S and K^{*0} mesons is almost constant as a function of p_T and consistent with unity showing that cold-nuclear-matter effects do not play a significant role in the measured kinematic range. A similar behavior is seen in $R_{d\rm Au}$ for all measured mesons. In the Cu + Cu collisions system, no nuclear modification is registered in peripheral collisions within the uncertainties of the measurement. In central Cu + Cu collisions, both mesons show suppression. In the range $p_T = 2$–5 GeV/c, the strange mesons show an intermediate suppression between the more suppressed π^0 and the nonsuppressed baryons. This behavior provides a particle species dependence of the suppression mechanism and provides additional constraints to the models

attempting to quantitatively reproduce nuclear modification factors. At higher p_T, all particles, π^0, strange mesons, and baryons, show a similar level of suppression.

ACKNOWLEDGMENTS

We thank the staff of the Collider-Accelerator and Physics Departments at Brookhaven National Laboratory and the staff of the other PHENIX participating institutions for their vital contributions. We acknowledge support from the Office of Nuclear Physics in the Office of Science of the Department of Energy, the National Science Foundation, Abilene Christian University Research Council, Research Foundation of SUNY, and Dean of the College of Arts and Sciences, Vanderbilt University (USA); Ministry of Education, Culture, Sports, Science, and Technology and the Japan Society for the Promotion of Science (Japan); Conselho Nacional de Desenvolvimento Científico e Tecnológico and Fundação de Amparo à Pesquisa do Estado de São Paulo (Brazil); Natural Science Foundation of China (P. R. China), Ministry of Science, Education, and Sports (Croatia); Ministry of Education, Youth and Sports (Czech Republic); Centre National de la Recherche Scientifique, Commissariat à l'Énergie Atomique, and Institut National de Physique Nucléaire et de Physique des Particules (France); Bundesministerium für Bildung und Forschung, Deutscher Akademischer Austausch Dienst, and Alexander von Humboldt Stiftung (Germany); OTKA Grant No. NK 101 428 and the Ch. Simonyi Fund (Hungary); Department of Atomic Energy and Department of Science and Technology (India); Israel Science Foundation (Israel); National Research Foundation of Korea of the Ministry of Science, ICT, and Future Planning (Korea); Physics Department, Lahore University of Management Sciences (Pakistan); Ministry of Education and Science, Russian Academy of Sciences, Federal Agency of Atomic Energy (Russia); VR and Wallenberg Foundation (Sweden); the US Civilian Research and Development Foundation for the Independent States of the Former Soviet Union; the Hungarian American Enterprise Scholarship Fund; and the US-Israel Binational Science Foundation.

[1] E. Shuryak, Phys. Rep. **61**, 71 (1980).
[2] M. Gyulassy and L. McLerran, Nucl. Phys. A **750**, 30 (2005); F. Karsch, Lect. Notes Phys. **583**, 209 (2002)
[3] See, e.g., Nucl. Phys. A **904-905**, 1c-1092c (2013).
[4] E. Braaten and M. H. Thoma, Phys. Rev. D **44**, R2625(R) (1991).
[5] D. d'Enterria and B. Betz, Lect. Notes Phys. **785**, 285 (2010).
[6] X. N. Wang and M. Gyulassy, Phys. Rev. Lett. **68**, 1480 (1992).
[7] A. Adcox *et al.* (PHENIX Collaboration), Phys. Rev. Lett. **88**, 022301 (2001).
[8] A. Adare *et al.* (PHENIX Collaboration), Phys. Rev. Lett. **101**, 162301 (2008).
[9] N. Armesto, J. Phys. G **32**, R367 (2006).
[10] J. W. Cronin *et al.*, Phys. Rev. D **11**, 3105 (1975).
[11] A. Adcox *et al.* (PHENIX Collaboration), Phys. Lett. B **561**, 82 (2003).
[12] S. S. Adler *et al.* (PHENIX Collaboration), Phys. Rev. Lett. **91**, 072301 (2003); A. Adare *et al.* (PHENIX Collaboration), *ibid.* **101**, 232301 (2008).
[13] S. S. Adler *et al.* (PHENIX Collaboration), Phys. Rev. C **69**, 034910 (2004).
[14] S. S. Adler *et al.* (PHENIX Collaboration), Phys. Rev. Lett. **96**, 202301 (2006).
[15] A. Adare *et al.* (PHENIX Collaboration), Phys. Rev. C **83**, 024909 (2011).
[16] C. Adler *et al.* (STAR Collaboration), Phys. Rev. Lett. **89**, 202301 (2002).
[17] C. Adler *et al.* (STAR Collaboration), Phys. Rev. Lett. **90**, 082302 (2003).
[18] J. Adams *et al.* (STAR Collaboration), Phys. Rev. Lett. **91**, 172302 (2003).
[19] J. Adams *et al.* (STAR Collaboration), Phys. Rev. Lett. **92**, 112301 (2004).
[20] S. Chatrchyan *et al.* (CMS Collaboration), Eur. Phys. J. C **72**, 1945 (2012).
[21] B. Abelev *et al.* (ALICE Collaboration), Phys. Lett. B **720**, 52 (2013).
[22] S. Chatrchyan *et al.* (CMS Collaboration), Phys. Rev. C **84**, 024906 (2011).
[23] S. Chatrchyan *et al.* (CMS Collaboration), Phys. Lett. B **712**, 176 (2012).
[24] G. Aad *et al.* (ATLAS Collaboration), Phys. Rev. Lett. **105**, 252303 (2010).
[25] A. Adare *et al.* (PHENIX Collaboration), Phys. Rev. C **84**, 044902 (2011).
[26] A. Adare *et al.* (PHENIX Collaboration), Phys. Rev. Lett. **98**, 172301 (2007).
[27] A. Adare *et al.* (PHENIX Collaboration), Phys. Rev. C **84**, 044905 (2011).
[28] G. Agakishiev *et al.* (STAR Collaboration), Phys. Rev. Lett. **108**, 072302 (2012).
[29] A. Adare *et al.* (PHENIX Collaboration), Phys. Rev. C **88**, 024906 (2013).
[30] S. S. Adler *et al.* (PHENIX Collaboration), Phys. Rev. Lett. **91**, 172301 (2003).
[31] S. S. Adler *et al.* (PHENIX Collaboration), Phys. Rev. C **69**, 034909 (2004).
[32] T. Hirano and Y. Nara, Phys. Rev. C **69**, 034908 (2004).
[33] R. J. Fries, V. Greco, and P. Sorensen, Annu. Rev. Nucl. Part. Sci. **58**, 177 (2008).
[34] S. Chatrchyan *et al.* (CMS Collaboration), Phys. Lett. B **724**, 213 (2013).
[35] ATLAS-CONF-2013-107.
[36] B. Abelev *et al.* (ALICE Collaboration), Phys. Lett. **110**, 082302 (2013).
[37] A. Adare *et al.* (PHENIX Collaboration), Phys. Rev. Lett **111**, 212301 (2013).
[38] A. Adare *et al.* (PHENIX Collaboration), Phys. Rev. D **83**, 052004 (2011).

[39] J. Adams *et al.* (STAR Collaboration), Phys. Rev. C **71**, 064902 (2005).
[40] B. I. Abelev *et al.* (STAR Collaboration), Phys. Rev. C **78**, 044906 (2008).
[41] M. M. Aggarwal *et al.* (STAR Collaboration), Phys. Rev. C **84**, 034909 (2011).
[42] K. Adcox *et al.* (PHENIX Collaboration), Nucl. Instrum. Methods A **499**, 469 (2003).
[43] K. Adcox *et al.* (PHENIX Collaboration), Nucl. Instrum. Methods A **497**, 263 (2003).
[44] M. Allen *et al.* (PHENIX Collaboration), Nucl. Instrum. Methods A **499**, 549 (2003).
[45] S. S. Adler *et al.* (PHENIX Collaboration), Phys. Rev. Lett. **94**, 082302 (2005).
[46] S. C. Johnson, Proceedings of the International Conference on Computing in High Energy Physics, CHEP 98, Chicago IL (unpublished).
[47] S. H. Aronson *et al.* (PHENIX Collaboration), Nucl. Instrum. Methods A **499**, 480 (2003).
[48] K. Adcox *et al.* (PHENIX Collaboration), Nucl. Instrum. Methods A **499**, 489 (2003).
[49] M. Aizawa *et al.* (PHENIX Collaboration), Nucl. Instrum. Methods A **499**, 508 (2003).
[50] A. Adare *et al.* (PHENIX Collaboration), Phys. Rev. C **83**, 064903 (2011).
[51] L. Aphecetche *et al.* (PHENIX Collaboration), Nucl. Instrum. Methods A **499**, 521 (2003).
[52] J. Beringer *et al.* (Particle Data Group), Phys. Rev. D **86**, 010001 (2012).
[53] S. S. Adler *et al.* (PHENIX Collaboration), Phys. Rev. C **76**, 034904 (2007).
[54] S. S. Adler *et al.* (PHENIX Collaboration), Phys. Rev. C **72**, 014903 (2005).
[55] A. Adare *et al.* (PHENIX Collaboration), Phys. Rev. C **81**, 034911 (2010).
[56] GEANT 3.2.1, CERN Computing Library (1993), http://wwwasdoc.web.cern.ch/wwwasdoc/pdfdir/geant.pdf.
[57] R. Glauber and G. Matthiae, Nucl. Phys. B **21**, 135 (1970).
[58] M. L. Miller, K. Reygers, S. J. Sanders, and P. Steinberg, Annu. Rev. Nucl. Part. Sci. **57**, 205 (2007).
[59] S. S. Adler *et al.* (PHENIX Collaboration), Phys. Rev. Lett. **98**, 172302 (2007).